J. Fluid Mech. (2010), *vol.* 660, *pp.* 430–455. © Cambridge University Press 2010
doi:10.1017/S0022112010002727

Numerical study of a vortex ring impacting a flat wall

MING CHENG[1], JING LOU[1] AND LI-SHI LUO[2]†

[1]Institute of High Performance Computing, 1 Fusionopolis Way, #16-16 Connexis, Singapore 138632, Singapore

[2]Department of Mathematics and Statistics and Center for Computational Sciences, Old Dominion University, Norfolk, VA 23529, USA

(Received 10 March 2009; revised 7 May 2010; accepted 8 May 2010; first published online 16 August 2010)

We numerically study a vortex ring impacting a flat wall with an angle of incidence $\theta \geqslant 0^\circ$ in three dimensions by using the lattice Boltzmann equation. The hydrodynamic behaviour of the ring–wall interacting flow is investigated by systematically varying the angle of incidence θ in the range of $0^\circ \leqslant \theta \leqslant 40^\circ$ and the Reynolds number in the range of $100 \leqslant Re \leqslant 1000$, where the Reynolds number Re is based on the translational speed and initial diameter of the vortex ring. We quantify the effects of θ and Re on the evolution of the vortex structure in three dimensions and other flow fields in two dimensions. We observe three distinctive flow regions in the θ–Re parameter space. First, in the low-Reynolds-number region, the ring–wall interaction dissipates the ring without generating any secondary rings. Second, with a moderate Reynolds number Re and a small angle of incidence θ, the ring–wall interaction generates a complete secondary vortex ring, and even a tertiary ring at higher Reynolds numbers. The secondary vortex ring is convected to the centre region of the primary ring and develops azimuthal instabilities, which eventually lead to the development of hairpin-like small vortices through ring–ring interaction. And finally, with a moderate Reynolds number and a sufficiently large angle of incidence θ, only a secondary vortex ring is generated. The secondary vortex wraps around the primary ring and propagates from the near end of the primary ring, which touches the wall first, to the far end, which touches the wall last. The rings develop a helical structure. Our results from the present study confirm some existing experimental observations made in the previous studies.

Key words: vortex flows, vortex instability, vortex interactions

1. Introduction

Vortex–wall interaction is ubiquitous in unsteady boundary-layer separation and wall-bounded turbulent flows. When a vortex is convected near a no-slip solid wall, it often instigates a viscous response in the vicinity of the wall (Saffman 1979; Lugt 1983; Kiya, Ohyama & Hunt 1986; Lim & Nickels 1995), which leads to various complicated flow phenomena. These phenomena include wall-generated vorticity, unsteady boundary separation, vertical-flow instability, separated vortex layer roll-up, as well as the interaction-induced aerodynamic forces on the wall. With a sufficiently

† Email address for correspondence: lluo@odu.edu

https://doi.org/10.1017/S0022112010002727 Published online by Cambridge University Press

high Reynolds number, vortex–wall interaction leads to vortex breakdown, which is an important mechanism in transition to turbulence. Flows with vortex–wall interaction have fascinated many for a long time because of their importance to our understanding of topological changes in evolving vortex structures and coherent structures in turbulence.

There have been numerous experimental and numerical studies of vortex rings impinging on a flat wall with a normal angle of incidence. Numerous experimental studies (Boldes & Ferreri 1973; Cerra & Smith 1983; Yamada *et al.* 1985; Walker *et al.* 1987; Lim, Nickels & Chong 1991; Chang 1992; Orlandi & Verzicco 1993; Chu, Wang & Hsieh 1993; Chu, Wang & Chang 1995; Swearingen, Crouch & Handler 1995; Fabris, Liepmann & Marcus 1996) have shown that, when a vortex ring approaches a solid wall, it induces a radial flow that, due to the no-slip condition at the wall, creates a boundary layer with vortices of opposite signs. The vortex ring expands its toroidal radius as it is closing in to the wall, while the vortex core shrinks, and the vorticity at the ring core is intensified due to vortex stretching. Subsequently, the boundary layer undergoes separation and growth, leading to ejection of vorticity. With a sufficiently large Reynolds number, a secondary vortex ring, and possibly a tertiary one, is generated from the boundary layer at the wall. The detailed velocity field and the stability of the secondary ring have been investigated numerically and through stability analysis for a vortex ring impacting a wall at normal incidence (Lim *et al.* 1991; Orlandi & Verzicco 1993; Chu *et al.* 1995; Swearingen *et al.* 1995; Chang, Hertzberg & Kerr 1997; Luton & Ragab 1997; Naguib & Koochesfahani 2004). Orlandi & Verzicco (1993) numerically studied the axisymmetric flow at $564 < Re < 3000$ and the fully three-dimensional flow at $Re = 1250$ to investigate the effects of azimuthal instabilities. They observed the high-wavenumber instabilities originating in the compression phase of the secondary ring within the primary one, and were able to explain the strong instability of the secondary ring by analysing the rate-of-strain tensor and vorticity alignment. Swearingen *et al.* (1995) studied both perturbed and unperturbed evolutions of the secondary ring with $Re \approx 645$. They analysed the linear evolution of the secondary vortex-ring instability by using a quasi-steady approximation and found that the secondary vortex ring is unstable when subject to long-wavelength perturbations. Chu *et al.* (1995) solved the Navier–Stokes equation by using the vorticity-streamfunction formulation for the axisymmetric flow with $500 \leqslant Re \leqslant 2000$ to obtain the wall-pressure distribution and total surface force on the wall. More recently, Naguib & Koochesfahani (2004) combined a velocimetry measurement with the solution of Poisson's equation for the axisymmetric flow to study the wall-pressure field and flow structures for an axisymmetric vortex ring impinging on a flat wall with $Re = 1860$. The flow behaviour of a vortex ring impacting on a flat wall with a normal incidence has been extensively studied experimentally, numerically and theoretically. Comprehensive reviews are given by Shariff & Leonard (1992), Lim & Nickels (1992), Doligaski, Smith & Walker (1994) and Verzicco & Orlandi (1996*b*).

While there has been a considerable number of studies on normal impacts of a vortex ring on a flat wall, little has been done for oblique impacts. The earliest work, to our knowledge, is an experimental study of a vortex ring impacting an inclined flat wall by Lim (1989), who observed the formation of bi-helical vortex lines around the circumferential axis of the ring on both sides of the symmetric plane perpendicular to the flat wall. Verzicco & Orlandi (1994) numerically investigated the same problem with the angle of incidence $\theta = 38.5^\circ$ and $Re = 600$. They showed that the secondary vorticity generated at the wall accumulates in the region of the ring furthest away

https://doi.org/10.1017/S0022112010002727 Published online by Cambridge University Press

from the wall and forms a vortex loop, which moves away from the wall. As the ring is closing in to the wall, the region which is touching the wall first (referred to as the 'near end' hereafter) is subjected to a strong stretching, which intensifies the vorticity in the core, while the region furthest away from the wall (referred to as the 'far end' hereafter) remains almost intact at the beginning of the ring–wall interaction process, provided that the oblique angle of incidence θ is sufficiently large. Consequently, the pressure is high at the near end, but low at the far end. The pressure gradient induces a convection along the toroidal axis from the near end to the far end, which is responsible for accumulating vorticity at the far end. A subsequent work of Mammetti, Verzicco & Orlandi (1999) confirmed the observations of Verzicco & Orlandi (1994) experimentally and numerically with $Re = 1000$. More recently, Liu (2002) used the vortex particle-in-cell method, a hybrid Eulerian–Lagrangian method, to simulate the unsteady shear flow induced by the interaction of a vortex ring and a flat wall with $\theta = 38.5^\circ$ and $Re = 600$ and 1000. Liu observed the development of the primary vortex ring and the pattern of the secondary vorticity generation, and compared the basic feature of the oblique impingement with the experimental results of Lim (1989). Liu also showed that, at a higher Reynolds number of 1000, the helical winding of vortex lines becomes more prominent, and the secondary vortex core is thicker. We note that most of the previous studies are restricted to a fixed angle of incidence θ and a very limited range of the Reynolds number Re. There is no systematic investigation on the dependence of the vortex–wall interaction, the evolution of vortex structures, and flow behaviour on both θ and Re.

In this work, we will systematically investigate the three-dimensional flow structures of a vortex ring impacting a flat wall with different angles of incidence and Reynolds numbers by using the lattice Boltzmann (LB) method (Yu *et al.* 2003). We intend to understand the mechanisms responsible for various flow phenomena induced by the vortex–wall interactions in the vortex-impinging flow by quantifying the effects of the impinging angle θ and the Reynolds number Re on the evolution of the flow fields around the ring–wall interaction region.

The remainder of this paper is organized as follows. In § 2, we provide a brief description of the lattice Boltzmann equation (LBE) with a multiple-relaxation-time (MRT) collision model (d'Humières 1992; Lallemand & Luo 2000, 2003; d'Humières *et al.* 2002) and relevant initial and boundary conditions. We validate our code by comparing the LB results with the existing results for the flow of a vortex ring impacting a wall at normal incidence, i.e. $\theta = 0^\circ$, and $Re = 830$ and 1000. A grid convergence study is carried out to ensure that an adequate mesh size is used in our simulations. In § 3, we present our results on the flow of a vortex ring impinging on a no-slip wall with the angle of incidence $0^\circ \leqslant \theta \leqslant 40^\circ$ and the Reynolds number $100 \leqslant Re \leqslant 1000$. We study the evolution of three-dimensional flow patterns and two-dimensional vorticity and pressure fields depending on θ and Re. Finally, we conclude the paper with a summary in § 4.

2. Numerical method

In this section we will briefly describe the LBE (cf. a review by Yu *et al.* 2003) with an MRT collision model (d'Humières 1992; Lallemand & Luo 2000, 2003; d'Humières *et al.* 2002). We will discuss the initial and boundary conditions for the flow of the vortex–wall interaction and their implementation in the LB simulations. We will also validate the model with existing data.

https://doi.org/10.1017/S0022112010002727 Published online by Cambridge University Press

2.1. *Lattice Boltzmann equation*

The LBE is derived from the Boltzmann equation to solve near-incompressible flows (He & Luo 1997*b*,*c*). We will use the generalized lattice Boltzmann equation (GLBE), or the LBE with the MRT collision model (d'Humières 1992; Lallemand & Luo 2000; d'Humières *et al.* 2002). The evolution equation for the MRT–LB model of Q velocities on a D-dimensional lattice $\boldsymbol{x}_i \in \delta_x \mathbb{Z}^D$ with discrete time $t_n \in \delta_t \mathbb{N}_0 := \delta_t\{0,\ 1, \ldots\}$ can be concisely written as

$$\boldsymbol{f}(\boldsymbol{x}_i + \boldsymbol{c}\delta_t, t_n + \delta_t) - \boldsymbol{f}(\boldsymbol{x}_i, t_n) = -\boldsymbol{M}^{-1} \cdot \hat{\boldsymbol{S}} \cdot \left[\boldsymbol{m} - \boldsymbol{m}^{(\mathrm{eq})}\right], \tag{2.1}$$

where $\boldsymbol{M}$ is a $Q \times Q$ matrix which linearly transforms the distribution functions $\boldsymbol{f} \in \mathbb{V} \equiv \mathbb{R}^Q$ to the velocity moments $\boldsymbol{m} \in \mathbb{M} \equiv \mathbb{R}^Q$,

$$\boldsymbol{m} = \boldsymbol{M} \cdot \boldsymbol{f}, \qquad \boldsymbol{f} = \boldsymbol{M}^{-1} \cdot \boldsymbol{m}, \tag{2.2}$$

and $\hat{\boldsymbol{S}}$ is a non-negative $Q \times Q$ diagonal relaxation matrix (d'Humières 1992; Lallemand & Luo 2000, 2003; d'Humières *et al.* 2002). The boldface symbols denote the following column vectors:

$$\left.\begin{aligned}
&\boldsymbol{f}(\boldsymbol{x}_i + \boldsymbol{c}\delta_t, t_n + \delta_t) = (f_0(\boldsymbol{x}_i, t_n + \delta_t), \ldots,\ f_b(\boldsymbol{x}_i + \boldsymbol{c}_b\delta_t, t_n + \delta_t))^{\mathrm{T}},\\
&\boldsymbol{f}(\boldsymbol{x}_i, t_n) = (f_0(\boldsymbol{x}_i, t_n),\ f_1(\boldsymbol{x}_i, t_n), \ldots,\ f_b(\boldsymbol{x}_i, t_n))^{\mathrm{T}},\\
&\boldsymbol{m} = (m_0(\boldsymbol{x}_i, t_n),\ m_1(\boldsymbol{x}_i, t_n), \ldots,\ m_b(\boldsymbol{x}_i, t_n))^{\mathrm{T}},\\
&\boldsymbol{m}^{(\mathrm{eq})} = \left(m_0^{(\mathrm{eq})}(\boldsymbol{x}_i, t_n),\ m_1^{(\mathrm{eq})}(\boldsymbol{x}_i, t_n), \ldots,\ m_b^{(\mathrm{eq})}(\boldsymbol{x}_i, t_n)\right)^{\mathrm{T}},
\end{aligned}\right\} \tag{2.3}$$

where T denotes the transpose operation and $b := (Q - 1)$.

In this paper, we use a nineteen-velocity model in three dimensions, denoted as the D3Q19 model (d'Humières *et al.* 2002). The discrete velocities of the model $\{\boldsymbol{c}_i | i = 0,\ 1, \ldots, 18\}$ are

$$\boldsymbol{c}_i = \begin{cases} (0,\ 0,\ 0)\,c, & i = 0,\\ (\pm 1, 0, 0)c,\ (0, \pm 1, 0)c,\ (0, 0, \pm 1)c, & i = 1, 2, \ldots, 6,\\ (\pm 1, \pm 1, 0)c,\ (\pm 1, 0, \pm 1)c,\ (0, \pm 1, \pm 1)c, & i = 7, 8, \ldots, 18, \end{cases} \tag{2.4}$$

where $c := \delta_x/\delta_t$. The specific ordering of moments used here for the D3Q19 model is (d'Humières *et al.* 2002; Lallemand & Luo 2003):

$$\boldsymbol{m} = (\rho, e, \varepsilon, j_x, q_x, j_y, q_y, j_z, q_z, 3p_{xx}, 3\pi_{xx}, p_{ww}, \pi_{ww}, p_{xy}, p_{yz}, p_{xz}, m_x, m_y, m_z)^{\mathrm{T}}, \tag{2.5}$$

where ρ is the mass density; $j_x = \rho u_x$, $j_y = \rho u_y$ and $j_z = \rho u_z$ are x, y and z components of the flow momentum $\boldsymbol{j} := \rho\boldsymbol{u}$, respectively, which are the conserved moments in the system. Other moments are non-conserved, and their equilibria are functions of the conserved moments ρ and $\rho\boldsymbol{u}$ in the system (d'Humières 1992; Lallemand & Luo 2000, 2003; d'Humières *et al.* 2002). With the above ordering of moments, the corresponding diagonal relaxation matrix of relaxation rates $\{s_i | i = 0, 2, \ldots, 18\}$, $s_i \in (0,\ 2)$, $\forall i$, is

$$\hat{\boldsymbol{S}} = \mathrm{diag}(0, s_1,\ s_2,\ 0,\ s_4,\ 0,\ s_4,\ 0,\ s_4,\ s_9,\ s_{10},\ s_9,\ s_{10},\ s_{13},\ s_{13}, s_{13},\ s_{16},\ s_{16}, s_{16}). \tag{2.6}$$

The parameters s_2, s_4, s_{10} and s_{16} do not have any direct effect on the large-scale hydrodynamic behaviour of the model; however, they must satisfy the stability criterion that $s_i \in (0,\ 2)\ \forall\, i$, and they can affect the stability of the model (Lallemand & Luo 2000; d'Humières *et al.* 2002). The values of these relaxation rates optimized for

https://doi.org/10.1017/S0022112010002727 Published online by Cambridge University Press

the linear stability (Lallemand & Luo 2000) are given by d'Humières *et al.* (2002): $s_1 = s_4 = 1.19$, $s_2 = s_{10} = 1.4$ and $s_{16} = 1.98$, which will be used in our simulations. The relaxation rates s_1 and $s_9 = s_{13}$ determine the bulk viscosity ζ and the shear viscosity ν, respectively. For the D3Q19 model with the particular ordering of moments given by (2.5), the transformation matrix $\boldsymbol{M}$ is given by d'Humières *et al.* (2002).

We can decompose the density ρ into its mean $\bar{\rho}$ and fluctuation $\delta\rho$, i.e.

$$\rho := \bar{\rho} + \delta\rho. \tag{2.7}$$

To reduce the effect of round-off error, we set $\bar{\rho} = 1$, and only consider the density fluctuation $\delta\rho$ in simulations. In addition, we use $\boldsymbol{j} = \bar{\rho}\boldsymbol{u}$ to reduce compressibility effects (He & Luo 1997*a*). Thus the conserved quantities in an 'athermal' LB model and the corresponding equilibria are

$$\delta\rho^{(\mathrm{eq})} = \delta\rho = \sum_i f_i, \quad \boldsymbol{j}^{(\mathrm{eq})} = \boldsymbol{j} := (j_x,\ j_y,\ j_z) = \bar{\rho}\boldsymbol{u} = \sum_i f_i \boldsymbol{c}_i. \tag{2.8}$$

For the athermal D3Q19 model in which the internal energy is not a conserved quantity, the equilibria for non-conserved moments are (d'Humières *et al.* 2002):

$$e^{(\mathrm{eq})} = -11\delta\rho + 19\left(j_x^2 + j_y^2 + j_z^2\right), \tag{2.9a}$$

$$\varepsilon^{(\mathrm{eq})} = -3\delta\rho - \frac{11}{3}\left(j_x^2 + j_y^2 + j_z^2\right), \tag{2.9b}$$

$$\boldsymbol{q}^{(\mathrm{eq})} = \left(q_x^{(\mathrm{eq})}, q_y^{(\mathrm{eq})}, q_z^{(\mathrm{eq})}\right) = -\tfrac{2}{3}(j_x, j_y, j_z), \tag{2.9c}$$

$$p_{xx}^{(\mathrm{eq})} = \tfrac{1}{3}\left[2j_x^2 - \left(j_y^2 + j_z^2\right)\right], \quad p_{ww}^{(\mathrm{eq})} = j_y^2 - j_z^2, \tag{2.9d}$$

$$p_{xy}^{(\mathrm{eq})} = j_x j_y, \quad p_{yz}^{(\mathrm{eq})} = j_y j_z, \quad p_{xz}^{(\mathrm{eq})} = j_x j_z, \tag{2.9e}$$

$$\pi_{xx}^{(\mathrm{eq})} = -\tfrac{1}{2} p_{xx}^{(\mathrm{eq})}, \quad \pi_{ww}^{(\mathrm{eq})} = -\tfrac{1}{2} p_{ww}^{(\mathrm{eq})}, \tag{2.9f}$$

$$m_x^{(\mathrm{eq})} = m_y^{(\mathrm{eq})} = m_z^{(\mathrm{eq})} = 0. \tag{2.9g}$$

With the above equilibria, the LB system of (2.1) leads to the incompressible Navier–Stokes equations in the limit of small Mach number and large system size (d'Humières *et al.* 2002; Junk, Klar & Luo 2005).

With the equilibria given by (2.9), the speed of sound c_s, the shear viscosity ν and the bulk viscosity ζ in the D3Q19 model are given by (Lallemand & Luo 2000; d'Humières *et al.* 2002; Lallemand & Luo 2003)

$$c_s = \frac{1}{\sqrt{3}}c, \quad \nu = \frac{1}{3}\left(\frac{1}{s_\nu} - \frac{1}{2}\right)c\delta_x, \quad \zeta = \frac{2}{9}\left(\frac{1}{s_\zeta} - \frac{1}{2}\right)c\delta_x, \tag{2.10}$$

where $s_\nu = s_9 = s_{13}$ and $s_\zeta = s_1$. The freedom to independently adjust the bulk viscosity $\zeta = \zeta(s_\zeta)$ is a primary reason for the superior stability of the MRT–LB models. For the D3Q19 model with the popular lattice Bhatnagar–Gross–Krook (BGK) collision model, $\zeta = 2\nu/3$. For high-Reynolds-number flows, the shear viscosity ν is very small, and the bulk viscosity in the lattice BGK model may be too small for the code to be stable. In contrast, the bulk viscosity ζ in the MRT–LB model is independent of the shear viscosity ν, and thus can remain as a constant to satisfy stability conditions (Lallemand & Luo 2000; d'Humières *et al.* 2002).

The LBE can be seen as a finite difference method with central-differencing and explicit time integration (Junk & Klar 2000; Junk 2001), and it is formally second-order accurate in space (Junk *et al.* 2005). The reasons for us to use the LBE in

https://doi.org/10.1017/S0022112010002727 Published online by Cambridge University Press

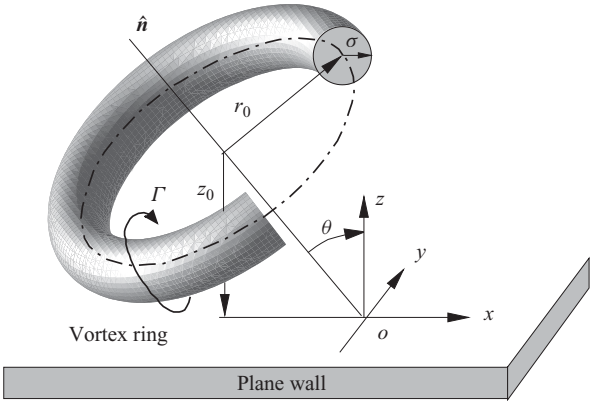


FIGURE 1. Schematic sketch of the geometry for a circular vortex ring approaching a plane wall.

this study are as follows. First, the LB algorithm is easy to implement. Secondly, the LB method is conservative, because both the collision and the advection processes, which are defined by the right-hand side and the left-hand side of (2.1), respectively, conserve mass and momentum exactly. In addition, the LB method has relatively low numerical dissipation and dispersion compared to conventional Navier–Stokes solvers of formally equal or even higher order of accuracy, as shown by using von Neumann analysis (Lallemand & Luo 2000, 2003; Marie, Ricot & Sagaut 2009). This is related, in part, to the fact that the LBE employs stencils larger than those used in conventional second-order schemes. For example, in two dimensions the minimum number of stencil points in the LBE is seven on a triangular lattice, and nine on a square lattice, as opposed to five for conventional computational fluid dynamics schemes on a square lattice. And finally, the code used in this study has been extensively validated and verified and has been proved to be an effective and efficient method for direct numerical simulations of vortex-dominated flows (Soo & Menon 2004; Cheng, Yao & Luo 2006; Cheng & Luo 2007; Cheng, Lou & Lim 2009; Peng *et al.* 2010).

2.2. *Flow configuration, boundary and initial conditions*

In this work, the dimensions of the computational domain in the x, y and z directions are L, W and H, respectively. The rectangular computational domain is discretized by a uniform mesh of size $N_x \times N_y \times N_z$, where N_x and N_y are two lateral dimensions of the mesh in two horizontal directions x and y, and N_z is the dimension in the vertical direction z. A vortex ring of radius r_0 is initially placed at a distance $z = z_0$ from a flat wall at $z = 0$, as illustrated in figure 1. The vortex ring is given a constant initial velocity that points to the flat wall with an angle θ.

The initial vorticity distribution of the vortex ring is assigned by a Gaussian function (Orlandi & Verzicco 1993), for which the velocity field is specified by the circulation Γ of the ring as follows:

$$\boldsymbol{u}_0 = \frac{\Gamma}{2\pi\sigma}\left[1 - \mathrm{e}^{-(\sigma/\sigma_0)^2}\right]\hat{\boldsymbol{\vartheta}}, \tag{2.11}$$

where $\hat{\boldsymbol{\vartheta}}$ is the unit vector tangential to circulation circles about the ring core, σ is the radial distance from the centre of the core, σ_0 is the initial core radius and $\sigma_0/r_0 = 0.21$. The initial translational speed of the ring can be estimated as

https://doi.org/10.1017/S0022112010002727 Published online by Cambridge University Press

(Lamb 1932)

$$u_s = \frac{\Gamma}{4\pi r_0}\left(\ln\frac{8r_0}{\sigma_0} - \frac{1}{4}\right). \tag{2.12}$$

No-slip boundary conditions are imposed for the flat wall located at $z=0$, which can be realized in the LBE by the bounce-back boundary conditions (d'Humières *et al.* 2002), in which all particles colliding with a solid wall reverse their momenta, i.e.

$$f_{\bar{i}} = f_i, \tag{2.13}$$

where $f_{\bar{i}}$ is the distribution function of the velocity $\boldsymbol{c}_{\bar{i}} := -\boldsymbol{c}_i$. The constant-pressure boundary conditions are applied at $x=0$, $x=L$, $y=0$, $y=W$ and $z=H$, by imposing the equilibrium distributions

$$f_i = f_i^{(\mathrm{eq})}(\rho = \bar{\rho}, \boldsymbol{u}), \tag{2.14}$$

where the constant-pressure condition is realized through the equation of state $p=\rho c_s^2$, and the velocity field $\boldsymbol{u}$ at boundaries is updated from the flow domain (Mussa, Asinari & Luo 2009; Verhaeghe, Luo & Blanpain 2009). Similarly, the initial conditions can be realized by imposing the following equilibrium distribution functions $f_i^{(\mathrm{eq})}(\bar{\rho}, \boldsymbol{u}_0)$, where $\boldsymbol{u}_0$ is given by (2.11).

We define the dimensionless position $\boldsymbol{R}$, vorticity $\boldsymbol{\Omega}$, time T, pressure P and Reynolds number Re, as follows:

$$\boldsymbol{R} := \frac{\boldsymbol{r}}{r_0}, \quad \boldsymbol{\Omega} := \frac{\boldsymbol{\omega} r_0^2}{\Gamma_0}, \quad T := \frac{\Gamma_0 t}{r_0^2}, \quad P := \frac{r_0^2(p-p_\infty)}{\bar{\rho}\Gamma_0^2}, \quad Re := \frac{2u_s r_0}{\nu}, \tag{2.15}$$

where $\boldsymbol{r}=(x, y, z)$ is the spatial vector in the Cartesian coordinates system, $\boldsymbol{\omega}=(\omega_x, \omega_y, \omega_z)$ is the vorticity and Γ_0 and u_s are the initial circulation and translational speed of the ring, respectively.

2.3. *Code validation*

We will validate our LB code by a comparison with the existing results for a vortex ring impacting a wall at normal incidence ($\theta=0°$) in viscous incompressible fluid (Walker *et al.* 1987; Verzicco & Orlandi 1994; Chu *et al.* 1995). The Gaussian ring is initially placed at the vertical position $z_0=3r_0$, where the initial conditions are determined experimentally (Chu *et al.* 1995).

We observe that as long as $L=W>10r_0$, where r_0 is the initial radius of the vortex ring (cf. figure 1), the effect due to a finite domain size is negligible. This observation is consistent with some of the previous results (Orlandi & Verzicco 1993; Liu 2002). We find that the computational domain size $L\times W\times H=12r_0\times 12r_0\times 7r_0$ is sufficiently large, and that a larger domain size changes the results very little. Therefore, we will use the computational domain size of $L\times W\times H=12r_0\times 12r_0\times 7r_0$ unless otherwise stated.

We conduct a grid convergence study using four different mesh sizes defined by the initial radius of the ring, $r_0=20\delta_x$, $25\delta_x$, $30\delta_x$ and $40\delta_x$, for the case of normal incidence ($\theta=0°$) and $Re=1000$. In figure 2, we show the grid-resolution dependence of the vorticity contours in the xz plane of symmetry at the times $T=6.0$ and $T=14.0$. As the resolution increases, the peak values of the vorticity on the symmetry plane, $|\Omega_y|_{max}$, corresponding to the four grid sizes, are 12.0427, 12.9219, 13.3654 and 13.5318 at $T=6.0$. When $T=14$, the values of $|\Omega_y|_{max}$ are 13.8214 and 14.0162, corresponding to resolutions of $r_0=30\delta_x$ and $40\delta_x$, respectively. By comparing the intensities and locations of the primary, secondary and tertiary vortices, as well as the small-scale

https://doi.org/10.1017/S0022112010002727 Published online by Cambridge University Press

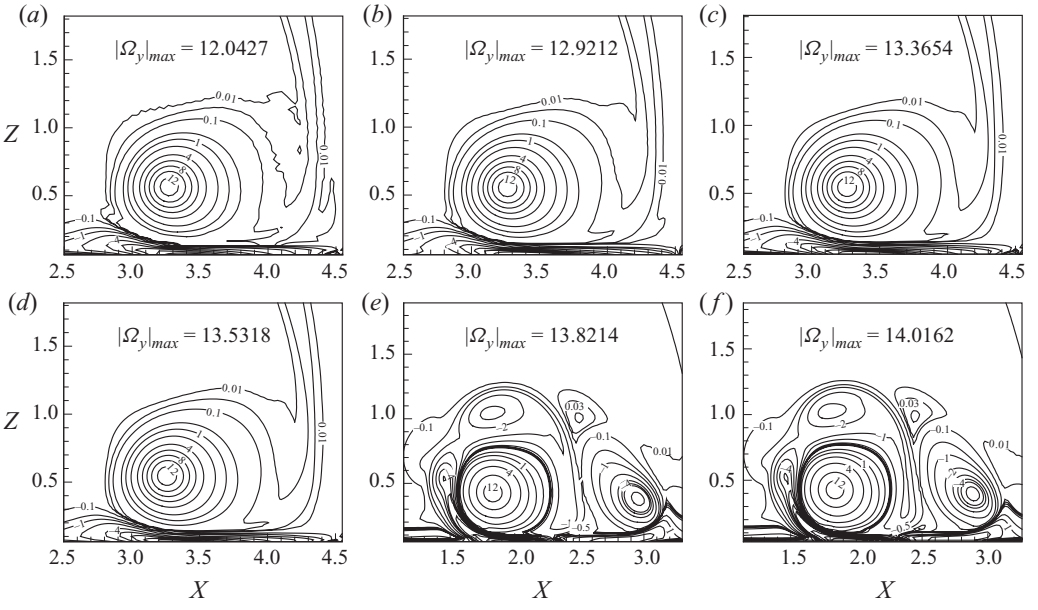


FIGURE 2. Comparison of vorticity contours in the xz plane of symmetry for a vortex ring impinging on a wall at $\theta = 0°$ and $Re = 1000$. (*a*) $r_0 = 20\delta_x$, $T = 6$; (*b*) $r_0 = 25\delta_x$, $T = 6$; (*c*) $r_0 = 30\delta_x$, $T = 6$; (*d*) $r_0 = 40\delta_x$, $T = 6$; (*e*) $r_0 = 30\delta_x$, $T = 14$; (*f*) $r_0 = 40\delta_x$, $T = 14$.

vortices, obtained by using these two meshes, we note that the quantitative differences in these results due to mesh size are small. For example, the value of $|\Omega_y|_{max}$ varies by less than roughly 2 % between $r_0 = 30\delta_x$ and $r_0 = 40\delta_x$. Unless otherwise stated, we will use the resolution $r_0 = 30\delta_x$ for the simulations in what follows.

We have also checked the effects on the results due to the aspect ratios of the computational domain and the perturbation wavenumber. We note that the perturbation of the azimuthal wavenumber four is generated naturally by the rectangular domain, although no initial perturbation is included in the simulations. The numerical perturbations of four-fold symmetry have been observed previously by Verzicco & Orlandi (1994, 1996*a*), and they do not affect essential features of the vortex flow at low Reynolds number $Re \leqslant 1000$, which we have also independently verified in this work. To investigate the effects due to perturbations, we carry out the simulations for the flow with $Re = 500$ and $\theta = 30°$ subjected to different perturbations. We add a sine wave perturbation in the azimuthal direction, with an amplitude $\epsilon = 0.02r_0 \approx 0.095\sigma_0$, and the wavenumber $n = 5$ and 6. We show, in figure 3, the vortex patterns for the unperturbed and perturbed flows at two different times, $T = 5$ and 20. We can see that the perturbations do not change essential large-scale flow features, such as the helical structure of the secondary vortex and the secondary vortex wrapping around the primary one. However, the perturbations do alter flow features on fine scales comparable to the wavelength of the perturbations and do so only at a late stage of the flow evolution. Because the perturbation of four-fold symmetry induced by the Cartesian domain is far weaker than the artificial perturbations, we can reasonably conclude that the effect induced by perturbations due to a Cartesian domain is negligible.

To further validate our code, we simulate the case of $\theta = 0°$ and $Re = 830$. The evolution of the vorticity iso-surface $\|\boldsymbol{\Omega}\| = 2.0$ in $5 \leqslant T \leqslant 15$ is shown in figure 4. Our

https://doi.org/10.1017/S0022112010002727 Published online by Cambridge University Press

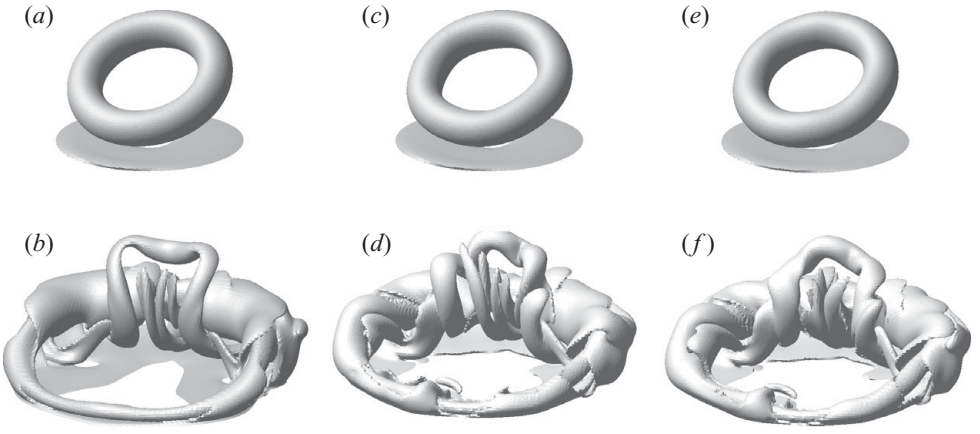


FIGURE 3. Vortex patterns for the flow with $Re = 500$ and $\theta = 30^\circ$ without and with perturbation at $T = 5$ (a,c,e) and 20 (b,d,f): without perturbation (a,b), and with a perturbation of the azimuthal wavenumber $n = 5$ (c,d) and $n = 6$ (e,f). The perturbation amplitude is $\epsilon = 0.02r_0 \approx 0.095\sigma_0$.

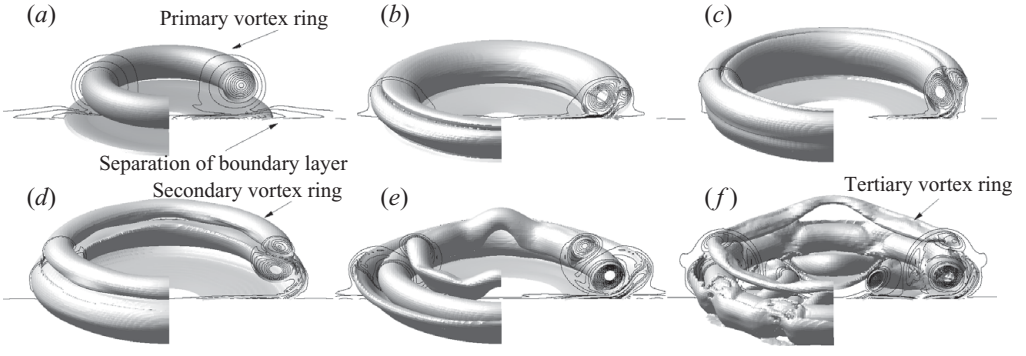


FIGURE 4. Evolution of vorticity iso-surface $\|\boldsymbol{\Omega}\| = 2.0$ for the case of $\theta = 0^\circ$ and $Re = 830$. (a) $T = 5$, (b) $T = 7$, (c) $T = 8$, (d) $T = 9$, (e) $T = 11$, (f) $T = 15$.

simulation clearly captures the generation of both secondary and tertiary vortex rings. In figure 5, we compare our numerical results with the experimental observations of Chu *et al.* (1995) in $3 \leqslant T \leqslant 11$. The essential flow features associated with the impingement of a vortex ring are accurately reproduced in our simulations, including the formation of the secondary vortex ring resulting from the roll-up of the separated boundary layer and the interaction between the primary and the secondary vortex rings. The agreement is further established quantitatively by the comparison of the trajectory of the primary vortex ring core with $Re = 830$ and 1000, as shown in figure 6. For the case of $Re = 1000$, figure 6 also shows the results obtained with three grid resolutions $r_0 = 20\delta_x$, $30\delta_x$ and $40\delta_x$. Clearly, the results are convergent to the experimental data. Overall, the LB results agree quantitatively with the experimental data of Chu *et al.* (1995).

3. Results and discussion

In this section we will present our findings for the flow of a vortex ring impacting on a flat wall with the angles of incidence $0^\circ \leqslant \theta \leqslant 40^\circ$ and the Reynolds numbers

https://doi.org/10.1017/S0022112010002727 Published online by Cambridge University Press

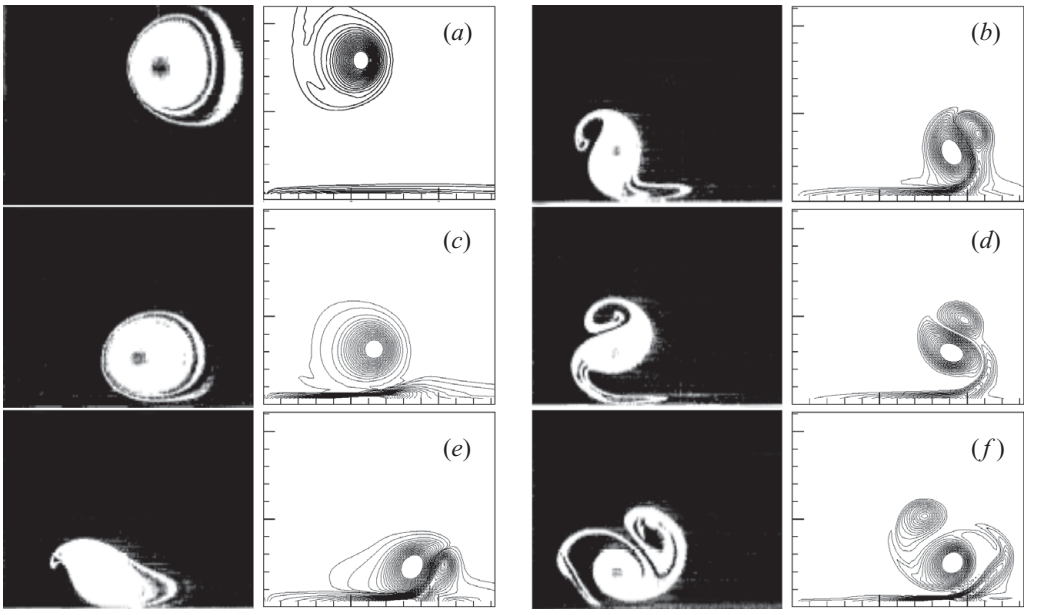


FIGURE 5. Evolution of the vortex ring patterns for the case of $\theta = 0°$ and $Re = 830$. The experimental data of Chu *et al.* (1995) (with black background) versus the LB results obtained in the present study (with white background). (*a*) $T = 3$, (*b*) $T = 8$, (*c*) $T = 5$, (*d*) $T = 9$, (*e*) $T = 7$, (*f*) $T = 11$.

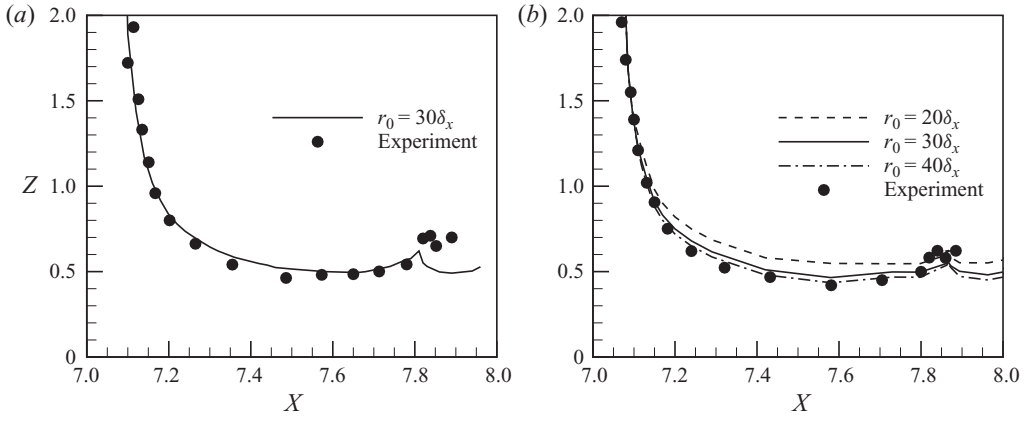


FIGURE 6. The trajectory of the primary ring centre for $Re = 830$ (*a*) and 1000 (*b*). The lines and symbols present the LB results obtained in this work and the experimental data of Chu *et al.* (1995), respectively.

$100 \leqslant Re \leqslant 1000$. The influence of the angle of incidence θ and the viscous effect of the fluid on the evolution of the vortex structure will be investigated by systematically varying θ and Re in their specified ranges. We will quantitatively analyse the dynamics of the flow by studying the evolutions of instantaneous vorticity and pressure fields, and other data generated in our simulations.

We will first present a three-dimensional vortex structure depending on the angle of incidence θ and the Reynolds number Re, in §§ 3.1 and 3.2, respectively, to qualitatively illustrate the evolution of the flow, followed by a more quantitative study of

https://doi.org/10.1017/S0022112010002727 Published online by Cambridge University Press

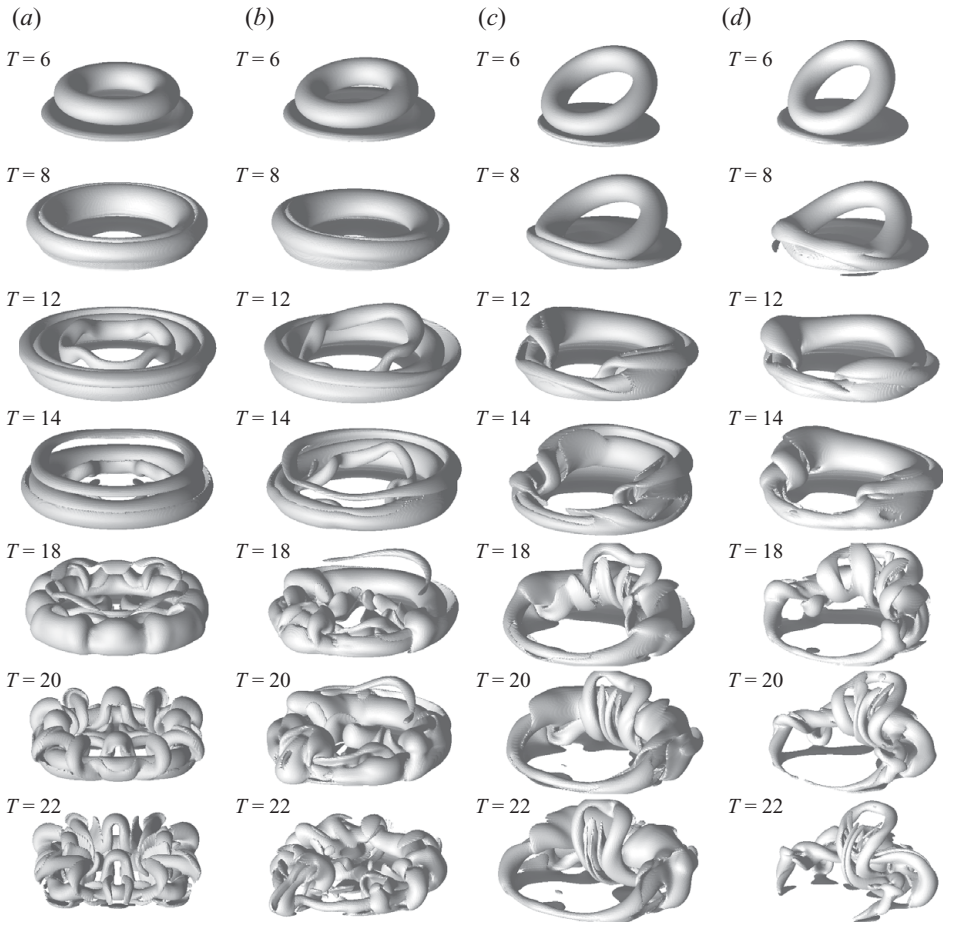


FIGURE 7. Dependence of the vortex structure evolution on the angle of incidence θ with a fixed Reynolds number $Re = 500$. The iso-surface of vorticity $\|\boldsymbol{\Omega}\| = 2$ is shown. (*a*) $\theta = 0°$, (*b*) $\theta = 10°$, (*c*) $\theta = 30°$, (*d*) $\theta = 40°$.

two-dimensional vorticity contours on the symmetric plane of the flow depending on θ and Re in §§ 3.3 and 3.4, respectively. We further present quantitative results on effects of θ and Re on the evolution of the vorticity at the vortex core, the trajectories of the primary vortex centres and the pressure distribution on the symmetric plane of the flow, in §§ 3.5, 3.6 and 3.7, respectively. We hope these results will collectively provide a coherent description of the flow.

3.1. *Effect of θ on the vortex structure*

We first show the dependence of flow patterns on the angle of incidence θ with a fixed Reynolds number Re. In figure 7 we show the evolutions of vorticity iso-surfaces with $Re = 500$ and $\theta = 0°$, 10°, 30° and 40°. The azimuthal symmetry of the flow is the most notable feature in the case of $\theta = 0°$, as shown in figure 7(*a*). A sequence of events takes place when the ring is moving close to the wall. First, the ring entrains surrounding fluids as it is closing in to the wall; and the flow starts to generate a thin boundary layer at the wall. Second, as the ring moves closer to the wall, it begins to stretch. And third, after $T \geqslant 6$, the boundary layer undergoes separation and rapid

https://doi.org/10.1017/S0022112010002727 Published online by Cambridge University Press

growth. As the flow further evolves, due to the radially adverse pressure gradient generated by the primary vortex ring at the wall and the local vorticity concentration within the boundary layer, a secondary vortex ring separates and lifts up from the wall. The interaction between the secondary vortex ring and the primary vortex ring decelerates the radial expansion of the primary ring and causes the primary ring to rebound from the wall. After $T = 8$, the secondary ring is convected inwards to the centre of the primary ring. It starts to develop azimuthal instabilities and becomes wavy at $T = 12$. At the same time, the primary ring further induces an additional separation of the boundary layer to generate a tertiary ring, which also rolls up from the wall, and is shed from the boundary at $T = 14$. Subsequently, the ring–ring and ring–wall interactions lead to complex three-dimensional topological changes in the flow. The flow starts to form a vortical structure that resembles hairpin vortices when $T = 20$. Figure 7(*a*) clearly captures the entire development process, in which a vortex ring evolves into multiple small-scale vortices. The vortex patterns shown in figure 7(*a*) are typical for the flow of normal impact ($\theta = 0^\circ$) with a moderate Reynolds number. Our results are consistent with previous observations (Walker *et al.* 1987; Verzicco & Orlandi 1994; Chu *et al.* 1995).

The flow with an oblique angle of incidence $\theta > 0^\circ$ is asymmetric about the axis of revolution of the ring. The complex ring–wall and ring–ring interactions for oblique impacts can be clearly seen from evolutions of vorticity iso-surfaces shown in figures 7(*b*), 7(*c*) and 7(*d*), corresponding to $\theta = 10^\circ$, 30° and 40°, respectively. As the vortex ring is closing in to the wall at an oblique angle, it induces an asymmetric shear layer on the wall. The shear layer first separates beneath the first impact point. When the near end of the ring contacts the wall, the boundary layer rapidly grows and the core of vortex ring is squeezed in the region about the impact point. This leads to an intense stretching of the ring in the region about the impact point, while the flow in the region away from the impact point is affected little, and thus remains almost intact. The stretching intensifies the vorticity, and therefore creates a non-uniform vorticity distribution along the core, so that the vorticity difference between the two opposite ends of the ring increases with the angle of incidence θ. Consequently, the non-uniform vorticity distribution generates a pressure gradient along the ring core, which pushes fluid away from the impact point along the circumference on both sides of the ring, as observed experimentally by Lim (1989). The shear layer induced near the wall rolls up an asymmetric secondary ring. However, this asymmetry does not significantly affect the overall vortex structure if the angle of incidence θ is small. For example, when $\theta = 10^\circ$, the secondary ring is convected inwards by the velocity field induced by the primary ring after $T = 8$. A weak tertiary ring is generated subsequently at $T = 14$, as seen in figure 7(*b*). As the ring–wall and ring–ring interaction develop, the vortex structure in the later stage of the impact ($T > 20$) is qualitatively similar to the case of $\theta = 0^\circ$, except for the asymmetry.

When the angle of incidence is increased to $\theta = 30^\circ$, no tertiary ring is generated. The secondary ring evolves in a manner that is completely different from the case of $\theta \leqslant 10^\circ$. With $\theta = 30^\circ$, the secondary vortex ring begins to wrap around the primary one at $T = 8$, as shown in figure 7(*c*). Later, the rings develop a helical structure, as observed by Lim (1989) and Verzicco & Orlandi (1994). For the case of $\theta = 40^\circ$, the vorticity evolution is rather similar to that for the case of $\theta = 30^\circ$ until $T = 20$. After $T > 20$, the ring begins to break up for $\theta = 40^\circ$, as shown in figure 7(*d*). In contrast, the ring maintains its integrity for $\theta = 30^\circ$ up to $T = 22$, as shown in figure 7(*c*). A more detailed discussion of this phenomenon will be given later in § 3.7.

https://doi.org/10.1017/S0022112010002727 Published online by Cambridge University Press

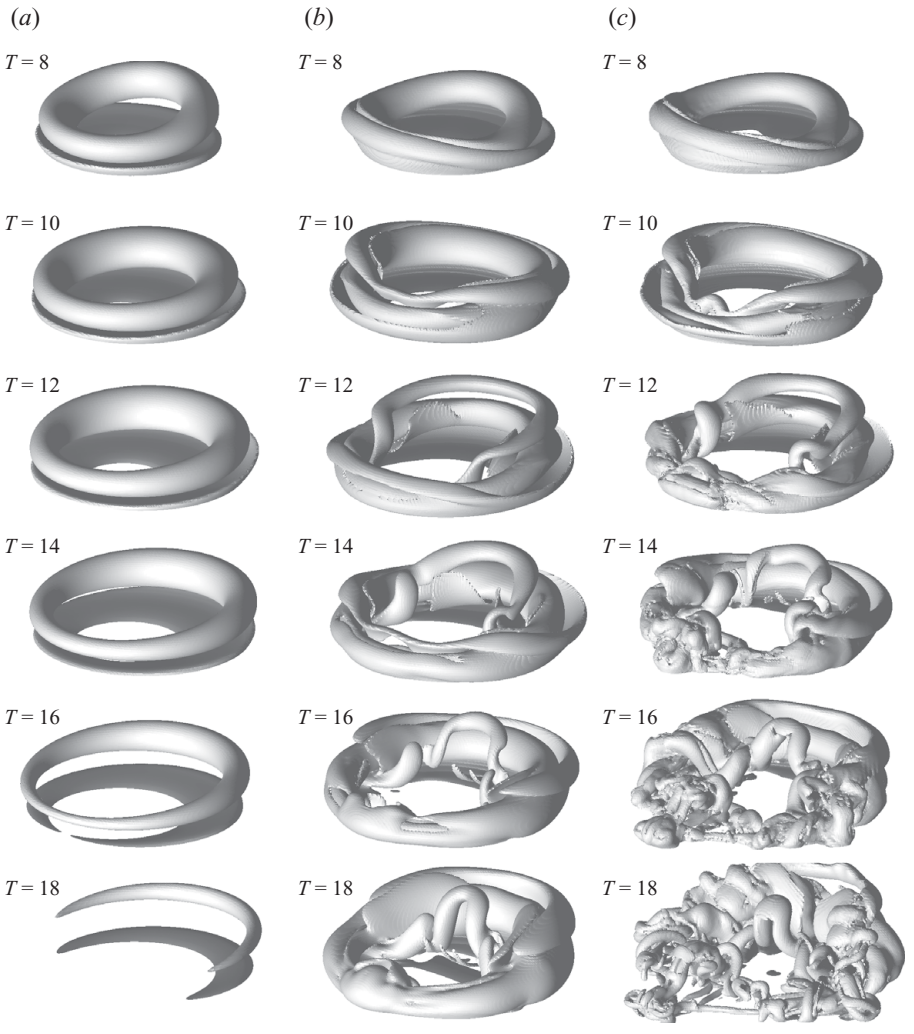


FIGURE 8. Dependence of the vortex structure evolution on the Reynolds number Re with a fixed angle of incidence $\theta = 20°$. The iso-surface of a constant vorticity $\|\boldsymbol{\Omega}\| = 2$ is shown. (*a*) $Re = 100$, (*b*) $Re = 500$, (*c*) $Re = 1000$.

3.2. *Effect of Re on the vortex structure*

We next report the dependence of flow patterns on the Reynolds number Re with a fixed angle of incidence θ. Figure 8 shows the flow patterns with $\theta = 20°$ and $Re = 100$, 500 and 1000. For the case of the lowest Reynolds number $Re = 100$, as shown in figure 8(*a*), the flow does not generate a secondary vortex ring. Although there is still a radial adverse pressure gradient, the detachment of the secondary vortex from the wall does not take place. At this low Reynolds number, the viscous effect diffuses vorticity and significantly weakens the circulation of the ring. The induced vorticity in the shear layer is quickly dissipated. The viscous force at the wall inhibits the radial expansion of the primary ring, and the vorticity at the wall is too weak to generate a secondary vortex ring. The vortex ring gradually decays into an arch vortex tube at $T = 18$, as shown in figure 8(*a*), before it is completely consumed by the viscous dissipation.

https://doi.org/10.1017/S0022112010002727 Published online by Cambridge University Press

As the Reynolds number increases, the viscous dissipation becomes weaker, and the vortex–wall interaction can trigger a series of complex responses in the boundary layer, as shown in figures 8(*b*) and 8(*c*) corresponding to $Re = 500$ and 1000, respectively. With $Re = 500$, the process of the secondary vortex ring wrapping around the primary ring appears, as shown in figure 8(*b*). The flow is complicated, but has a well-organized loop-like structure. When the Reynolds number is further increased to 1000, the flow pattern becomes considerably more complicated, especially after $T = 14$, as shown in figure 8(*c*). Small-scale vortices are generated by the interaction between the secondary vortex ring and the primary one. When $T = 18$, the core of the primary ring starts to break down. Vortex pairs of different sizes are generated, and vortical loops wrapping around the wavy inner core region are developed, as shown in figure 8(*c*). After $T \geqslant 18$, the flow structure at $Re = 1000$ has gone through a sequence of complicated topological changes and becomes rather complex with vortices of various sizes.

Our observations can be summarized as follows. With a finite angle of incidence $10^\circ \leqslant \theta \leqslant 40^\circ$ and a moderate Reynolds number $100 < Re \leqslant 1000$, the primary vortex ring generates secondary and tertiary rings; the secondary ring develops azimuthal instabilities, and in turn small-scale vortices are generated due to interactions among the vortex rings. The flow structure undergoes a series of complicated topological changes during the evolution process. As the angle of incidence increases beyond a critical value depending on the Reynolds number Re, the primary vortex ring generates only the secondary ring, which will wrap around the primary one, and then both rings will evolve to a helical structure later in the process. For example, with $Re = 500$, we do not observe any tertiary vortices when $\theta \geqslant 20^\circ$. With the angle of incidence fixed at $\theta = 20^\circ$, our results show that, as the Reynolds number increases, the flow around the primary vortex ring becomes more and more unstable. Beyond a critical Reynolds number of about 200, the flow begins to develop the helical winding around the circumferential axis of the ring, which appears earlier in time and becomes stronger as the Reynolds number increases beyond the critical value about 200. Our results clearly show that the evolution of the vortex–wall interaction strongly depends on both the Reynolds number Re and the angle of incidence θ.

3.3. *Effects of θ on vorticity and unsteady shear layer*

In this and the following sections, we will study the evolution of the flow by examining the vorticity contours in the xz plane of symmetry with different angles of incidence and Reynolds numbers, as shown in figures 9 and 10. These figures show instantaneous vorticity distributions of the rings and the shear layer on the wall, which allow us to quantitatively analyse the dynamics of vortex ring evaluation.

We first investigate the effects of the angle of incidence θ on the vorticity. Figure 9 shows the evolution of vorticity with $Re = 500$ and $\theta = 0^\circ$, 10° and 30°, corresponding to the simulations shown in figures 7(*a*), 7(*b*) and 7(*c*), respectively. For the case of a normal impact, i.e. $\theta = 0^\circ$, figure 9(*a*) clearly illustrates the radial expansion of the primary ring in a radial direction and the production of secondary and tertiary vortex rings. The primary ring expands radially rather rapidly in the initial stage of the impact during $6 \leqslant T \leqslant 8$. The radial expansion slows down during $8 \leqslant T \leqslant 10$ and almost comes to a halt later. The diameter of the primary ring varies from $2.2r_0$ at $T = 4$, to $2.51r_0$ at $T = 6$, $3.49r_0$ at $T = 8$, and $3.56r_0$ at $T = 10$. Further, the radial growth rate is about 0.2 in $4 \leqslant T \leqslant 6$, 0.5 in $6 \leqslant T \leqslant 8$ and 0.1 at $T = 10$. The variations in the radial expansion rate correspond to different stages of the impact process. As the vortex ring moves closer the wall when $T \leqslant 6$, the entrained fluid forces the ring to expand its diameter rather quickly, while the core of the ring shrinks so that the

https://doi.org/10.1017/S0022112010002727 Published online by Cambridge University Press

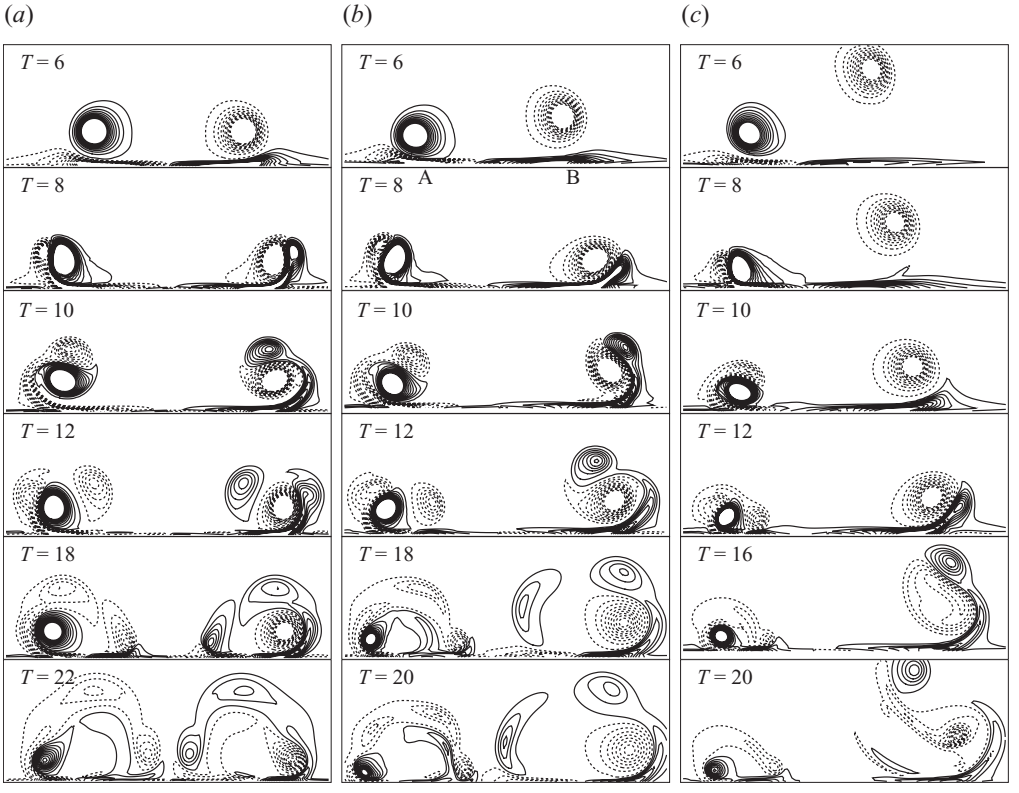


FIGURE 9. Dependence of the vorticity contours in the xz plane of symmetry on the angle of incidence θ with a fixed Reynolds number $Re = 500$, corresponding to figure 7. Positive and negative vorticity are represented by solid and dashed lines, respectively. Contours are plotted in the range of $|\Omega_y| \leqslant 5$ with a level interval of $\Delta\Omega_y = 0.5$. (*a*) $\theta = 0°$, (*b*) $\theta = 10°$, (*c*) $\theta = 30°$.

total volume of the ring is preserved. When the ring hits and then interacts strongly with the wall in $6 \leqslant T \leqslant 8$, the boundary layer grows rapidly and then separates; the radially adverse pressure gradient helps to eject the vorticity to form a secondary vortex ring. Because the circulation of the secondary ring is opposite to that of the primary ring, the flow induced by the secondary ring decelerates the radial expansion of the primary ring. The primary ring rebounds from the wall while interacting with the secondary ring; the interaction between the primary and secondary rings also leads to cancellation of their vorticity. The vorticity ratio of the secondary to primary rings in their centres decreases monotonically in time: from 0.68 at $T = 8$, to 0.39 at $T = 10$ and then to 0.22 at $T = 18$. As the secondary ring is convected inwardly by the flow field which has been induced by the primary ring, its detachment from the wall forms a sheet wrapping around the primary ring and, later, an elongated region of concentrated secondary vorticity. A tertiary vortex ring is generated when $T \approx 18$. The process of generating new subvortex rings does not continue indefinitely, because the strength of the primary vortex is continuously weakened by viscous dissipation during the ring–wall and ring–ring interactions. Both the core size and the vorticity strength at core centre of the primary ring decrease in time; when $T = 22$, the core size and the vorticity strength are reduced by 50 % and 60 %, respectively. The subvortex generation would take place only when the primary ring is strong enough, that is, in the early stage of the impact. Although the secondary ring also impacts the wall and

https://doi.org/10.1017/S0022112010002727 Published online by Cambridge University Press

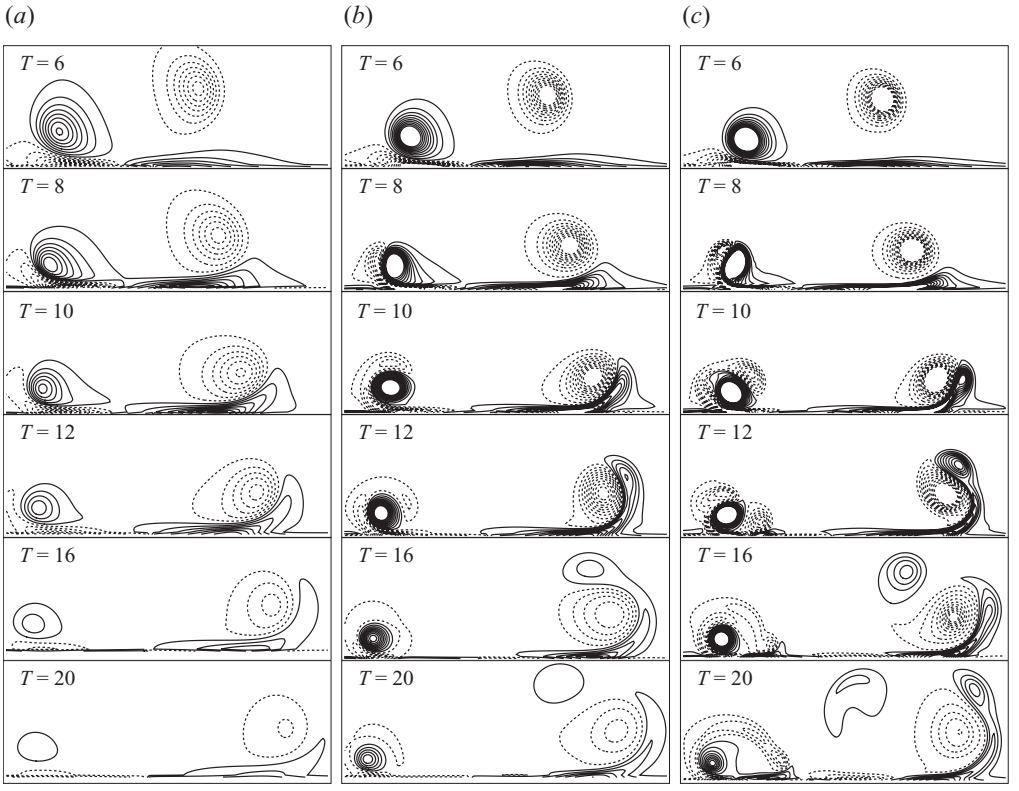


FIGURE 10. Dependence of the vorticity contours in the xz plane of symmetry on the Reynolds number Re with a fixed angle of incidence $\theta = 20°$, corresponding to figure 8. Positive and negative vorticity are represented by solid and dashed lines, respectively. (*a*) $Re = 100$, (*b*) $Re = 250$, (*c*) $Re = 500$.

ejects vorticity from the wall, it is too weak to generate a new subring. The secondary ring is eventually absorbed into the boundary layer, as is clearly shown in figure 9(*a*).

With the angle of incidence $\theta = 10°$, the overall flow evolution is similar to that of $\theta = 0°$, apart from the lack of the perfect rotational symmetry, as shown in figure 9(*b*). With this small angle of incidence, the time delay between the near end and far end of the ring impinging on the wall is not long enough to qualitatively alter the flow pattern. The evolution of the ring diameter follows the same trend as that of $\theta = 0°$. The radial expansion is rather rapid during the initial stage of the impact, then slows down after the secondary vortex ring is fully formed. The rate of the radial expansion varies from about 0.2 in $4 \leqslant T \leqslant 6$, to 0.4 in $6 \leqslant T \leqslant 8$, and finally 0.15 at $T = 10$. In contrast to the case of normal impact, shown in figure 9(*a*), the radial expansion for the case of $\theta = 10°$ is slightly slower when the ring is touching the wall, but is faster after the ring bounces from the wall, as shown in figure 9(*b*). With an oblique angle of incidence, the plane of the ring is tilted with respect to the wall; therefore, the expansion force is reduced because it has a component normal to the wall at the near end, which is blocked by the wall. Consequently, the vortex core at the first impact point is compressed and the vorticity is intensified, while the radial expansion force is weakened. The boundary-layer separation and the ejection of secondary vorticity take place earlier at the near end, marked by 'A' in figure 9(*b*), than at the far end of the ring, marked by 'B' in figure 9(*b*). The radial expansion is still going on at the far end, but has stopped at the near end. Also, the ring can expand more freely at the

https://doi.org/10.1017/S0022112010002727 Published online by Cambridge University Press

far end because it tilts upwards, away from the wall, while the opposite is true at the near end. As a result, the radial expansion is slightly slower at first, and then slightly faster after $T = 8$, than the case of normal incidence.

When the angle of incidence is increased to $\theta = 30^\circ$, the essential flow features are qualitatively different from those with smaller angles of incidence $\theta \leqslant 10^\circ$, because the time delay between the near end and the far end impacting the wall is considerably longer now. As shown in figure 9(c), the times when the near end and the far end touch the wall are about $T = 6$ and 10, respectively. During this time period of $6 \leqslant T \leqslant 10$, the ring core at the near end is severely compressed and the vorticity at the core centre is strengthened by 20 %. Due to intense stretching, the core becomes so thin that the ring cannot produce a secondary vortex to be shed from the wall. Instead, it generates small-scale vortices at the wall, which form a vorticity layer around the near end. Subsequent interaction between the secondary vorticity layer and the primary ring leads to cancellation of vorticity, hence weakens vorticity. When $T = 10$, the far end of the ring impacts the wall and the ring expands radially faster, because the expansion force tilts upwards with the angle θ with respect to the wall, and thus is not impeded by the wall. Subsequently, a secondary vortex is generated which then moves around the primary ring from the bottom upwards away from the wall. The radial expansion rate varies from about 0.18 in $6 \leqslant T \leqslant 8$, to 0.32 in $8 \leqslant T \leqslant 10$ and to 0.2 at $T = 16$.

We observe that the radial expansion rate during the impact decreases as the oblique angle θ increases. When the primary ring impacts on the wall, a vorticity gradient is generated roughly along its core axis, which affects not only the vorticity strength of the primary ring, but also the vortex structure, as shown in figures 7(b) and 7(c). This vorticity gradient is the driving mechanism responsible for the secondary vortex wrapping around the primary ring.

3.4. *Effects of Re on vorticity and unsteady shear layer*

We now investigate the effect of the Reynolds number Re on the flow with a fixed angle of θ. Figure 10 shows the vorticity evolution at a fixed angle of $\theta = 20^\circ$ and $Re = 100$, 250 and 500 to demonstrate the effect due to the Reynolds number alone. Clearly, the higher the Reynolds number, the weaker the viscous dissipation; hence the stronger the primary vortex when the ring impacts the wall. The secondary vortex is generated only when the Reynolds number is larger than a critical value depending on the angle of incidence θ. We estimate that the critical Reynolds numbers corresponding to $\theta = 10^\circ$ and 20° are about 100 and 200, respectively. As the Reynolds number further increases beyond the critical value, the secondary vortex becomes stronger, moves faster and detaches from the wall sooner, as is clearly shown in figures 10(b) and 10(c). There are several competing forces in the flow: the radial expansion force induced by the fluid entrained to the middle of the ring, the pressure gradient due to the non-uniform vorticity distribution along the ring circumference, the friction on the wall, and the viscous force in the flow. These forces all strongly depend on both the Reynolds number and the angle of incidence, and it is the competition among these forces that leads to the complex flow phenomena.

3.5. *Evolution of the vorticity at the vortex core*

We show, in figure 11, the evolution of the y component of the vorticity, Ω_y, and its normalized rate of change, $(\mathrm{d}\Omega_y/\mathrm{d}T)/\Omega_y$, at the primary vortex centres on the xz plane of symmetry for $Re = 100$ and 500 and with $\theta = 0^\circ$, 10° and 30°. When

https://doi.org/10.1017/S0022112010002727 Published online by Cambridge University Press

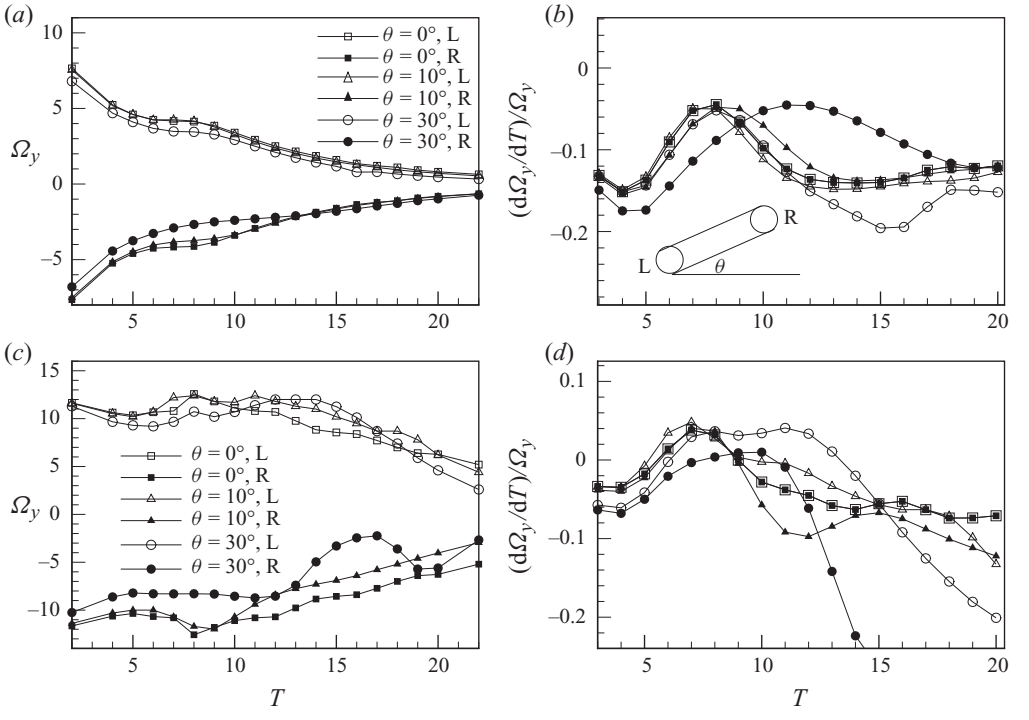


FIGURE 11. Time evolution of the vorticity and its rate of change at the centre of primary ring in the xz plane of symmetry at different θ. (a, b) $Re = 100$, (c, d) $Re = 500$.

the Reynolds number $Re = 100$, as shown in figures 11(a) and 11(b), for Ω_y and $(\mathrm{d}\Omega_y/\mathrm{d}T)/\Omega_y$, respectively, the angle of incidence θ has little effect on the vorticity values at the ring centres. Only for the case of $\theta = 30°$ can the asymmetry of the flow be clearly seen in the evolution of the vortex-centre vorticities. The values of Ω_y at the vortex centres of the near end and the far end behave similarly: their magnitudes $|\Omega_y|$ at the near-end and far-end vortex centres decrease monotonically in time, with a faster rate initially (until $T = 5$), then at a slower rate. The evolution of the vorticity magnitudes depends very weakly on the angle of incidence θ, because viscous dissipation dominates the flow at low Reynolds numbers.

With $Re = 500$, the flow is qualitatively different from the case of $Re = 100$, as shown in figures 11(c) and 11(d). The evolution of the vorticity magnitudes depends strongly on the angle of incidence θ in this case. The asymmetry of the flow is clearly seen, and the evolution of the vorticity magnitudes is no longer monotonic. With $\theta \leqslant 10°$, the magnitudes of Ω_y at the two vortex centres on the xz plane first decrease up to $T = 5$, then increase, and after attaining their maxima at about $T = 8$, they decrease again at slower rates. With $\theta = 30°$, the magnitude of Ω_y at the near-end core centre (labelled 'L' in the figure 11) first decreases before $T = 5$, then increases very slowly until $T = 12$, and then decreases at a faster rate. The magnitude of Ω_y at the far-end core centre (labelled 'R' in figure 11) first goes through irregular decrease–increase oscillations, then reaches a maximum which is very close to its initial value at about $T = 14$, when the secondary vortex ring is about to detach from the wall, and finally decays monotonically after $T > 14$. The fact that at $T = 14$ the magnitude of Ω_y at the far-end core centre almost recovers to its initial value indicates that vorticity is indeed transported to the far end, as discussed previously.

https://doi.org/10.1017/S0022112010002727 Published online by Cambridge University Press

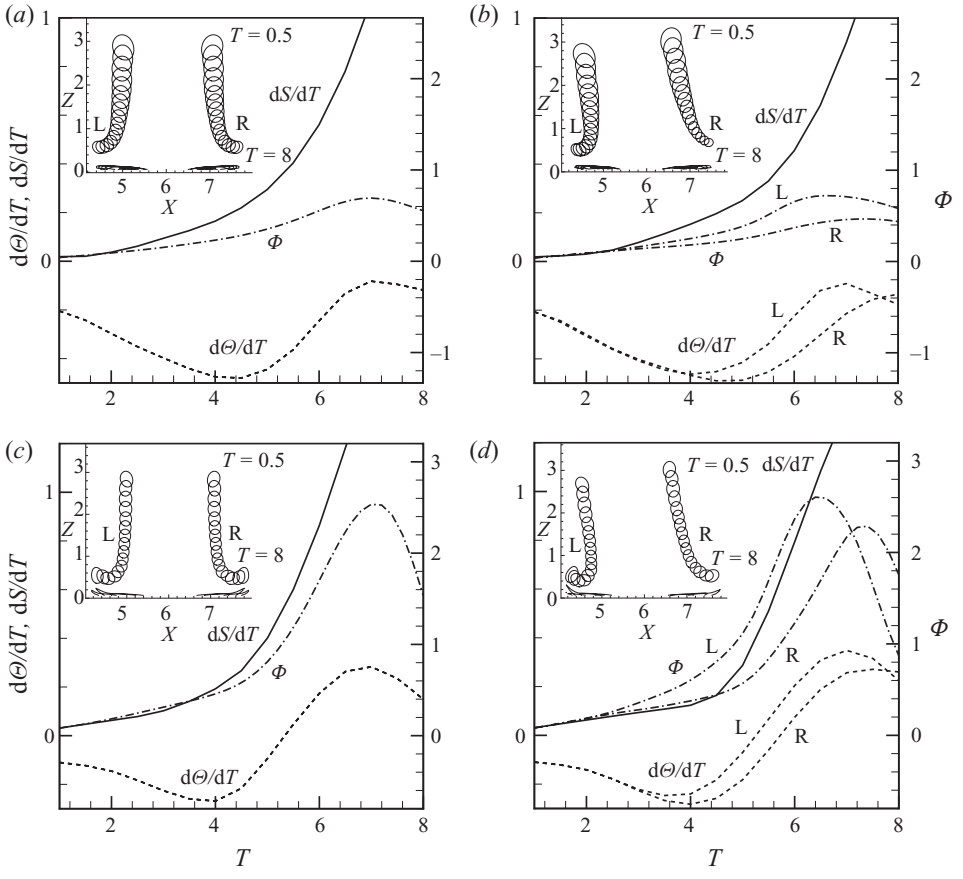


FIGURE 12. The dynamics of vortex stretching and ring expansion at the near end and far end of the ring, with $Re = 100$ and 500 and $\theta = 0°$ and 10°. We compute $\mathrm{d}S/\mathrm{d}T$, $\mathrm{d}\Theta/\mathrm{d}T$ and Φ as functions of time T at the near end and far end of the vortex ring. (*a*, *b*) $Re = 100$ and the vortex ring is defined by $\|\boldsymbol{\Omega}\| = 3.5$; (*c*, *d*) $Re = 500$ and the vortex ring is defined by $\|\boldsymbol{\Omega}\| = 7.5$. (*a*, *c*) $\theta = 0°$; (*b*, *d*) $\theta = 10°$.

To quantitatively study the dynamics of vortex stretching and ring core expansion, we compute the following quantities at the near end and far end of the ring: (i) the rate of change of the ring core circumference, $\mathrm{d}S/\mathrm{d}T$, where $S = \pi D$ is the ring circumference and D is the ring diameter; (ii) the rate of change of the centre vorticity strength Θ, $\mathrm{d}\Theta/\mathrm{d}T$; and (iii) $\Phi := \hat{\boldsymbol{s}} \cdot (\boldsymbol{\Omega} \cdot \nabla)\boldsymbol{u}$, where $\hat{\boldsymbol{s}}$ is the unit vector along the ring core. We first define a 'vortex ring', which is a torus, by using a constant iso-surface $\|\boldsymbol{\Omega}\| = \text{constant}$, and circumference S is defined by the centre core of the torus. On the symmetric xz plane, the contour of $\|\boldsymbol{\Omega}\| = \text{constant}$ defines the area A of the ring cross-section, and we use $\Theta = \boldsymbol{\Omega} \cdot \hat{\boldsymbol{s}} A = |\Omega_y| A$ to approximate the ring-centre vorticity strength at the both ends of the ring. On the symmetric xz plane of the ring, we also have

$$\Phi = \hat{\boldsymbol{s}} \cdot (\boldsymbol{\Omega} \cdot \nabla)\boldsymbol{u} = (\hat{\boldsymbol{y}} \cdot \hat{\boldsymbol{s}})(\boldsymbol{\Omega} \cdot \nabla)u_y, \tag{3.1}$$

which is directly related to the vortex stretching $\boldsymbol{\Omega} \cdot (\boldsymbol{\Omega} \cdot \nabla)\boldsymbol{u}$. In figure 12 we show the results of $\mathrm{d}S/\mathrm{d}T$, $\mathrm{d}\Theta/\mathrm{d}T$ and Φ at the near end and far end for $0 \leqslant T \leqslant 8$ with $Re = 100$ and 500, and $\theta = 0°$ and 10°. The stretching is slower initially, as is shown by the dynamics of $\mathrm{d}S/\mathrm{d}T$ and Φ, and the vorticities at the near end and far end are weakened monotonically by the viscous effect to reach their minima during this period

https://doi.org/10.1017/S0022112010002727 Published online by Cambridge University Press

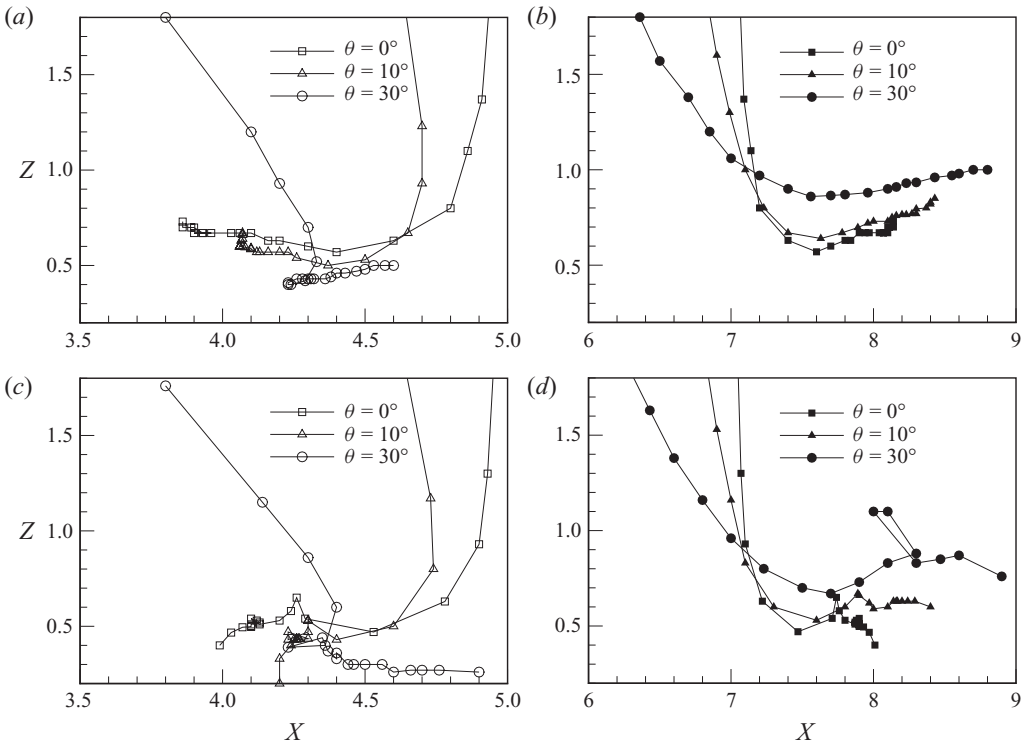


FIGURE 13. The trajectory of the vorticity centres of the primary ring in the xz plane of symmetry at different θ. The hollow and solid symbols denote the centres at the near end (a,c) and the far end (b,d), respectively. $Re = 100$ (a,b) and 500 (c,d).

of time, as shown by the dynamics of $\mathrm{d}\Theta/\mathrm{d}T$. As the ring moves closer to the flat plate, the ring expands radially with a faster rate, while the vorticities at both the near end and far end strengthen until they reach their maxima and then weaken again (cf. figure 11). The higher the Reynolds number is, the weaker is the viscous resistance force; hence the faster the ring approaches the plate, the sooner $\mathrm{d}\Theta/\mathrm{d}T$ reaches its minimum, as is clearly seen in figure 12. Also, the higher the Reynolds number is, the greater is the variation of $\mathrm{d}\Theta/\mathrm{d}T$, and the more asymmetric $\mathrm{d}\Theta/\mathrm{d}T$ becomes when $\theta > 0°$.

We observe that $\mathrm{d}\Theta/\mathrm{d}T$ remains negative when $Re = 100$, indicating viscous dissipation is the dominant effect. When $Re = 500$, $\mathrm{d}\Theta/\mathrm{d}T$ is negative initially but becomes positive after $T > 5$, indicating thickening of the ring about its core, i.e. increase of σ, when the ring is closing in to the flat plate. After reaching its peak, $\mathrm{d}\Theta/\mathrm{d}T$ is expected to decay and becomes negative eventually. The vorticity stretching related quantity Φ increases monotonically to its peak and then decays monotonically; and Φ peaks at approximately the same times as $\mathrm{d}\Theta/\mathrm{d}T$. The dynamics of $\mathrm{d}S/\mathrm{d}T$, $\mathrm{d}\Theta/\mathrm{d}T$, and Φ all consistently corroborate with that of the vorticity Ω_y shown in figure 11.

3.6. *Trajectories of the primary vortex centres*

The trajectories of the primary vortex centres in the xz plane of symmetry with $Re = 100$ and 500 and different θ are shown in figure 13. With $Re = 100$, most trajectories move down first and then outwards and slightly up, except for the near-end centre with $\theta = 30°$. With $\theta = 30°$, after moving down and outwards, the near-end centre moves inwards to the ring centre due to collective effects of the viscous force

https://doi.org/10.1017/S0022112010002727 Published online by Cambridge University Press

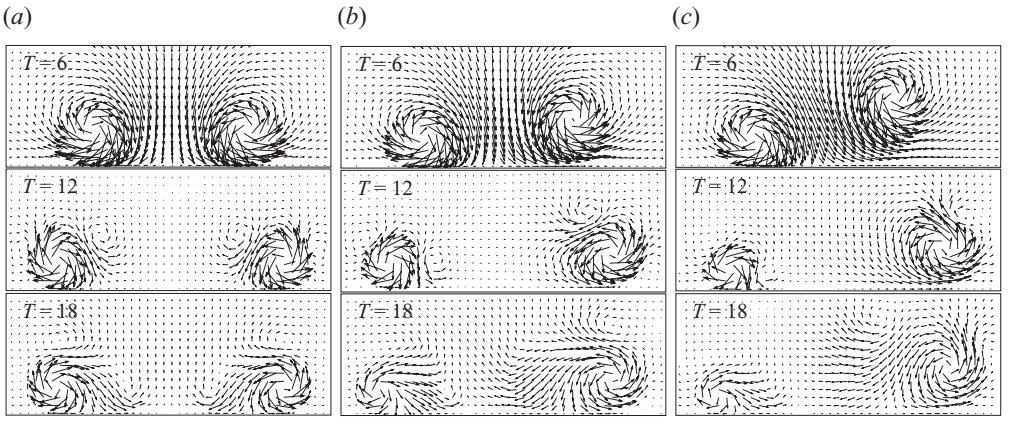


FIGURE 14. The θ-dependence of the velocity field on the xz plane of symmetry for $Re = 500$. (a) $\theta = 0°$, (b) $\theta = 10°$, (c) $\theta = 20°$.

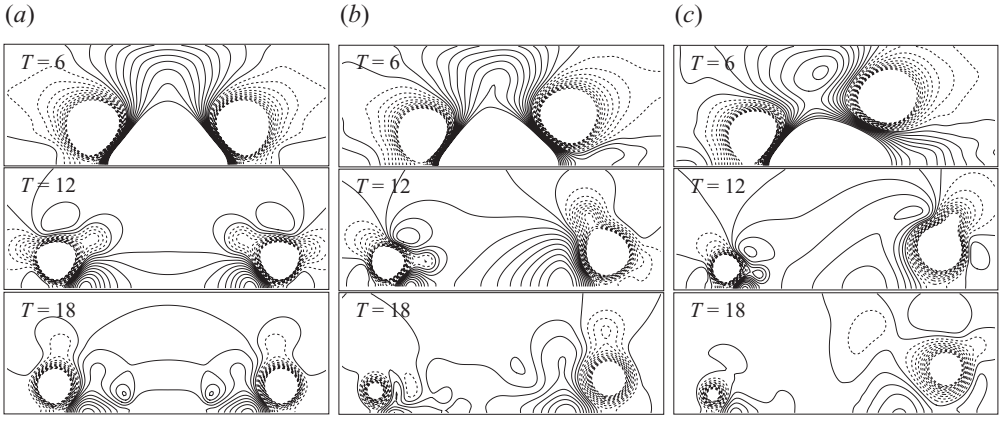


FIGURE 15. The θ-dependence of the pressure field on the xz plane of symmetry for $Re = 500$, corresponding to the velocity field in figure 14. Solid and dotted lines represent the positive (pushing) and negative (suction) pressures, respectively. The pressure contours are plotted in the range of $|P| \leqslant 0.1$ with a level interval of $\Delta P = 0.01$. (a) $\theta = 0°$, (b) $\theta = 10°$, (c) $\theta = 20°$.

and the adverse pressure gradient along the toroidal axis, which inhibit the ring expansion and weaken the vorticity at the near end. The lowest positions reached by the vortex core centres depend on the angle of incidence θ. The vortex core centre reaches its lowest position $Z_{min} = 0.52$, 0.46 and 0.38 at the near end, and $Z_{min} = 0.52$, 0.61 and 0.82 at the far end, for $\theta = 0°$, 10° and 30°, respectively.

With $Re = 500$, the vortex centre trajectories are more complicated because of the secondary vortex rings, which are absent in the case of $Re = 100$. The interaction between the primary and secondary vortex rings results in non-monotonous motion of the vorticity centres, shown as kinks and loops in figures 13(c) and 13(d).

3.7. *Pressure distribution*

Figures 14 and 15 show the evolution of the velocity field and the pressure contours, respectively, on the xz plane of symmetry with a fixed Reynolds number $Re = 500$ and $\theta = 0°$, 10° and 20°. The velocity and pressure fields are directly correlated to

https://doi.org/10.1017/S0022112010002727 Published online by Cambridge University Press

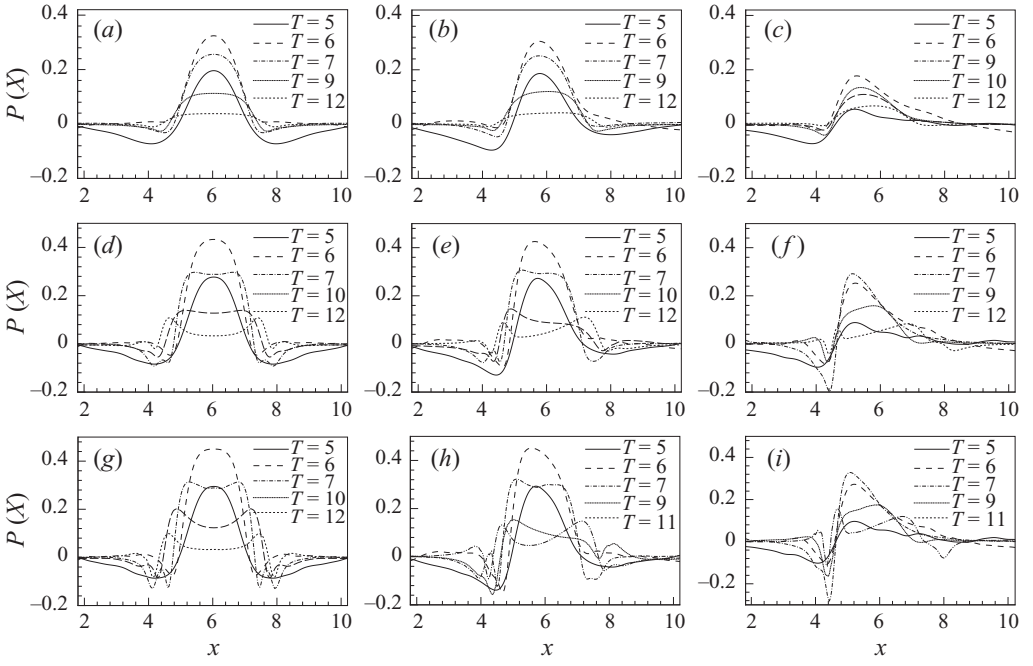


FIGURE 16. Dependence of the pressure distribution $P(X)$ on the wall surface and along the x-axis in the xz plane of symmetry on Re and θ. $Re = 100$ (a–c), $Re = 500$ (d–f), and $Re = 1000$ (g–i). (a,d,g) $\theta = 0°$, (b,e,h) $\theta = 10°$, (c,f,i) $\theta = 30°$.

the vorticity field shown in figures 9 and 10. The negative pressure resides mostly in the core regions of the ring. The pressure is high in high-strain regions and low in high-vorticity regions. It is the vortex–wall and/or vortex–vortex interactions that generate high strain rates, which in turn generate positive pressure. Strong flows develop around the vortex core due to the pressure gradient between intense and weak vorticity regions. The low-pressure region shrinks as the primary ring decelerates and decays. The deceleration is the result of both viscous dissipation and entrainment of surrounding fluids. As the angle of incidence θ increases, the flow becomes more asymmetric; the vorticity is more intense at the far end and weaker at the near end. The disparity between the vortex strengths at the two ends depends on both the angle of incidence θ and the Reynolds number Re.

For an oblique impact, a pressure gradient along the ring core generates a convective motion responsible for the transport of the secondary vorticity from the near end of the ring to the far end. Therefore, the behaviour observed previously in figures 7(b) and 7(c) can be explained as follows. When the ring interacts with the wall, the stretching is different along the core due to the asymmetry of the flow: the stretching rate in the near-end region is higher than that at the far end, hence a pressure gradient along the toroidal axis is generated. This pressure gradient induces a convection from the near-end region to the far-end region, resulting in an accumulation of secondary vorticity in the far-end region and the formation of a vortex loop, which moves away from the wall. In the mean time, viscous diffusion is accompanied with the fluid motion driven by the pressure gradient, which weakens vorticity, and eventually breaks the primary ring in the near-end region.

The evolution of the pressure distribution $P(X)$ on the wall surface along the x-axis on the xz plane of symmetry is presented in figure 16 for $Re = 100$, 500 and 1000, and

https://doi.org/10.1017/S0022112010002727 Published online by Cambridge University Press

	θ		
Re	0°	10°	30°
100	0.326	0.305	0.183
500	0.442	0.421	0.294
1000	0.475	0.452	0.321

TABLE 1. Dependence of the maximum stagnation pressure on θ and Re, corresponding to figure 16.

$\theta = 0°$, 10° and 30°. For all the cases with different θ and Re shown in figure 16, the pressure distribution $P(X)$ on the wall surface shows quantitatively one of the most prominent features of the flow: the radially adverse pressure gradient at the centre of the ring, which is responsible for the radial expansion of the ring.

For the case of low Reynolds number $Re = 100$, when the ring approaches the wall, it induces a region of radially adverse pressure gradient on the wall, which is clearly shown in the top row of figure 16. This pressure gradient does not significantly affect the overall characteristics of the flow structure because the viscous diffusion quickly destroys vorticity at this low Reynolds number. The interaction between the primary vortex ring and the wall does not produce any secondary rings. As the angle of incidence θ increases, the maximum value of the pressure at the stagnation point decreases, and the suction pressure increases on the near end and decreases on the far end.

With $Re = 500$, the results of $P(X)$ are shown in the middle row of figure 16. The variation of pressure on the wall at $\theta = 0°$ is similar to the observation of Chu *et al.* (1995). As shown in the figure, the pressure reaches its maximum value in the ring centre at $T \approx 6$, when the primary vortex ring is in its early stage of stretching. Meanwhile, a region of adverse pressure gradient develops, which alters the existing vorticity distribution in the boundary layer and has a significant effect on its later development. Rapid variations of the pressure gradients in the regions of $3 < X < 5$ and $7 < X < 9$ are associated with the boundary layer separation and the formation of secondary vortices. This is correlated with the ring–wall interaction shown in figure 10. As the angle of incidence θ increases, the stagnation moves to the near end of the ring. The stagnation pressure reduces by about one third, from 0.44 to 0.29, when θ increases from 0° to 30°. We note that the magnitude of pressure variations increases significantly at the near end and decreases at the far end as the angle of incidence θ increases.

The pressure distribution $P(X)$ at $Re = 1000$ is shown in the bottom row of figure 16. Comparing with the results of lower Reynolds numbers, we can clearly see that magnitudes of both the stagnation pressure and the variation of the pressure gradients in the regions of the ring–wall interaction increase as Re increases. The values of the maximum pressure on the wall at different θ and Re are summarized in table 1.

4. Conclusions

In this work, we numerically study the vortex ring impacting a flat wall with an oblique angle of incidence $0° \leqslant \theta \leqslant 40°$ and the Reynolds number $100 \leqslant Re \leqslant 1000$. We quantify the effects of both the Reynolds number Re and the angle of incidence

https://doi.org/10.1017/S0022112010002727 Published online by Cambridge University Press

θ on the evolution of the vortex structure and the hydrodynamic forces on the wall. We present the vortex structure in three dimensions, the vorticity contours on the symmetric xz plane of the ring–wall flow, the evolution of the vortex centre vorticities, the trajectories of vortex centres, the pressure and velocity fields on the symmetric xz plane and the wall-surface pressure distribution $P(X)$ along the x-axis. Our results not only confirm the initial structure of secondary vortex formation and shedding observed previously, but also reveal some interesting three-dimensional features of the flow of vortex ring–wall interaction with a oblique angle of incidence θ.

There are several competing factors interacting in the flow of a vortex ring impinging on a flat wall: the radially adverse pressure gradient induced by the fluid entrained by the ring in the proximity of the wall, the vortex stretching, the boundary layer generated by the ring–wall interaction, the pressure and vorticity gradients along the ring diameter due to oblique asymmetry and, finally, the viscous dissipation. The interactions among these forces lead to the following scenarios. First, in the low-Reynolds-number region $Re < 100$, the ring–wall interaction dissipates the ring. No secondary rings are generated. Second, when the Reynolds number is moderately high, i.e. $Re > 100$ and for oblique angles of incidence $0^\circ \leqslant \theta < 20^\circ$, the flow generates a secondary ring, and even a tertiary one at higher Reynolds numbers and smaller angle of incidence. The asymmetry due to the non-zero angle of incidence does not alter the essential feature of the flow. The secondary ring rolls up and is convected inwards to the centre area of the primary ring. The secondary ring develops azimuthal instabilities when the Reynolds number is sufficiently high, and the ring–ring interaction generates hairpin-like small-scale vortices in the late stage of the evolution. Finally, when the oblique angle of incidence θ is large enough and the Reynolds number is moderately high, a vorticity gradient is generated along the diameter of the ring between the near-end and the far-end regions. This gradient strengthens the vorticity at the far-end region at the expense of vorticity at the near-end region. The flow develops a helical structure winding around the circumferential axis of the primary ring, the secondary ring wraps around the primary one and they bounce away from the wall before a tertiary ring can be created. This structure of the secondary vortexes wrapping around the primary ring is fundamentally different from the structure with tertiary rings at a smaller angle of incidence. With a sufficiently large angle of incidence θ, due to the vorticity gradient, the vorticity propagation along the ring diameter is so strong that the vorticity at the near end of the primary ring is completely consumed during the impact process. Consequently, the primary ring breaks up and becomes an arc.

In conclusion, the flow of a vortex ring interacting with a flat wall has exhibited rich dynamic behaviours which strongly depend on both the Reynolds number Re and the angle of incidence θ. Within the parameter ranges of $100 \leqslant Re \leqslant 1000$ and $0^\circ \leqslant \theta \leqslant 40^\circ$, we observe a range of interesting flow phenomena including viscous decay, generation of secondary vortex rings, instabilities due to vortex–wall and vortex–vortex interactions, vortex breaking and reconnection. These observations will help us extend our understanding of flows with vortex–wall interactions in more complicated circumstances.

The authors are grateful to Dr S. P. Quan and Professor T. T. Lim for helpful discussions and comments, and Mr John Gounley for his editorial assistance. We would also like to thank the anonymous referees, whose comments helped improve this paper significantly.

https://doi.org/10.1017/S0022112010002727 Published online by Cambridge University Press

REFERENCES

Boldes, U. & Ferreri, J. C. 1973 Behavior of vortex rings in the vicinity of a wall. *Phys. Fluids* **16** (11), 2005–2006.

Cerra, A. W. & Smith, C. R. 1983 Experimental observations of vortex ring interaction with the fluid adjacent to a surface. *Tech. Rep.* FM-4. Department of Mechanical Engineering and Mechanics, Lehigh University.

Chang, C. C. 1992 Potential flow and forces for incompressible viscous flow. *Proc. R. Soc. Lond.* A **437** (1901), 517–525.

Chang, T. Y., Hertzberg, J. R. & Kerr, R. M. 1997 Three-dimensional vortex/wall interaction: entrainment in numerical simulation and experiment. *Phys. Fluids* **9** (1), 57–66.

Cheng, M. & Luo, L.-S. 2007 Characteristics of two-dimensional flow around a rotating circular cylinder near a plane wall. *Phys. Fluids* **19** (6), 063601.

Cheng, M., Lou, J. & Lim, T. T. 2009 Motion of a vortex ring in a simple shear flow. *Phys. Fluids* **21** (8), 081701.

Cheng, M., Yao, Q. & Luo, L.-S. 2006 Simulation of flow past a rotating circular cylinder near a plane wall. *Intl J. Comput. Fluid Dyn.* **20** (6), 391–400.

Chu, C. C., Wang, C. T. & Chang, C. C. 1995 A vortex ring impinging on a solid plane surface-vortex structure and surface force. *Phys. Fluids* A **7** (6), 1391–1401.

Chu, C. C., Wang, C. T. & Hsieh, C. S. 1993 An experimental investigation of vortex motions near surfaces. *Phys. Fluids* A **5** (6), 662–676.

Doligaski, T. L., Smith, C. R. & Walker, J. D. A. 1994 Vortex interactions with walls. *Annu. Rev. Fluid Mech.* **26**, 573–616.

Fabris, D., Liepmann, D. & Marcus, D. 1996 Quantitative experimental and numerical investigation of a vortex ring impinging on a wall. *Phys. Fluids* **8** (10), 2640–2649.

He, X. & Luo, L.-S. 1997*a* Lattice Boltzmann model for the incompressible Navier–Stokes equation. *J. Stat. Phys.* **88** (1/2), 927–944.

He, X. & Luo, L.-S. 1997*b* A priori derivation of the lattice Boltzmann equation. *Phys. Rev.* E **55** (6), R6333–R6336.

He, X. & Luo, L.-S. 1997*c* Theory of lattice Boltzmann method: from the Boltzmann equation to the lattice Boltzmann equation. *Phys. Rev.* E **56** (6), 6811–6817.

d'Humières, D. 1992 Generalized lattice-Boltzmann equations. In *Rarefied Gas Dynamics: Theory and Simulations* (ed. B. D. Shizgal & D. P. Weave), Progress in Astronautics and Aeronautics, vol. 159, pp. 450–458. AIAA.

d'Humières, D., Ginzburg, I., Krafczyk, M., Lallemand, P. & Luo, L.-S. 2002 Multiple-relaxation-time lattice Boltzmann models in three dimensions. *Phil. Trans. R. Soc. Lond.* A **360** (1792), 437–451.

Junk, M. 2001 A finite difference interpretation of the lattice Boltzmann method. *Numer. Methods Part. Differ. Equ.* **17** (4), 383–402.

Junk, M. & Klar, A. 2000 Discretizations for the incompressible Navier–Stokes equations based on the lattice Boltzmann method. *SIAM J. Sci. Comput.* **22** (1), 1–19.

Junk, M., Klar, A. & Luo, L.-S. 2005 Asymptotic analysis of the lattice Boltzmann equation. *J. Comput. Phys.* **210** (2), 676–704.

Kiya, K., Ohyama, M. & Hunt, J. C. R. 1986 Vortex pairs and rings interacting with shear-layer vortices. *J. Fluid Mech.* **172**, 1–15.

Lallemand, P. & Luo, L.-S. 2000 Theory of the lattice Boltzmann method: dispersion, dissipation, isotropy, Galilean invariance, and stability. *Phys. Rev.* E **61** (6), 6546–6562.

Lallemand, P. & Luo, L.-S. 2003 Lattice Boltzmann method for moving boundaries. *J. Comput. Phys.* **184** (2), 406–421.

Lamb, H. 1932 *Hydrodynamics*. Cambridge University Press.

Lim, T. T. 1989 An experimental study of a vortex ring interacting with an inclined wall. *Exp. Fluids* **7** (7), 453–463.

Lim, T. T. & Nickels, T. B. 1992 Instability and reconnection in the head-on collision of two vortex rings. *Nature* **357** (6375), 225–227.

Lim, T. T. & Nickels, T. B. 1995 Vortex rings. In *Fluid Vortices: Fluid Mechanics and its Applications* (ed. S. I. Green), chapter IV, pp. 95–153. Kluwer.

https://doi.org/10.1017/S0022112010002727 Published online by Cambridge University Press

Lim, T. T., Nickels, T. B. & Chong, M. S. 1991 A note on the cause of rebound in the head-on collision of a vortex ring with a wall. *Exp. Fluids* **12** (1/2), 41–48.

Liu, C. H. 2002 Vortex simulation of unsteady shear flow induced by a vortex ring. *Comput. Fluids* **31** (2), 183–207.

Lugt, H. J. 1983 *Vortex Flow in Nature and Technology*. Wiley.

Luton, J. A. & Ragab, S. A. 1997 The three-dimensional interaction of a vortex pair with a wall. *Phys. Fluids* **9** (10), 2967–2980.

Mammetti, M., Verzicco, R. & Orlandi, P. 1999 The study of vortex ring/wall interaction for artificial nose improvement. *ESAIM: Proc.* **7**, 258–269.

Maríe, S., Ricot, D. & Sagaut, P. 2009 Comparison between lattice Boltzmann method and Navier–Stokes high-order schemes for computational aeroacoustics. *J. Comput. Phys.* **228** (4), 1056–1070.

Mussa, A., Asinari, P. & Luo, L.-S. 2009 Lattice Boltzmann simulations of 2D laminar flows past two tandem cylinders. *J. Comput. Phys.* **228** (4), 983–999.

Naguib, A. M. & Koochesfahani, M. M. 2004 On wall-pressure sources associated with the unsteady separation in a vortex-ring/wall interaction. *Phys. Fluids* **16** (7), 2613–2622.

Orlandi, P. & Verzicco, R. 1993 Vortex rings impinging on walls: axisymmetric and three-dimensional simulations. *J. Fluid Mech.* **256**, 615–646.

Peng, Y., Liao, W., Luo, L.-S. & Wang, L.-P. 2010 Comparison of the lattice Boltzmann and pseudo-spectral methods for decaying turbulence: low-order statistics. *Comput. Fluids* **39** (4), 568–591.

Saffman, P. G. 1979 The approach of a vortex pair to a plane surface in inviscid fluid. *J. Fluid Mech.* **92**, 497–503.

Shariff, K. & Leonard, A. 1992 Vortex rings. *Annu. Rev. Fluid Mech.* **24**, 235–279.

Soo, J. H. & Menon, S. 2004 Simulation of vortex dynamics in three-dimensional synthetic and free jets using the large-eddy lattice Boltzmann method. *J. Turbul.* **5**, 032.

Swearingen, J. D., Crouch, J. D. & Handler, R. A. 1995 Dynamics and stability of a vortex ring impacting a solid boundary. *J. Fluid Mech.* **297**, 1–28.

Verhaeghe, F., Luo, L.-S. & Blanpain, B. 2009 Lattice Boltzmann modeling of microchannel flow in slip flow regime. *J. Comput. Phys.* **228** (1), 147–157.

Verzicco, R. & Orlandi, P. 1994 Normal and oblique collisions of a vortex ring with a wall. *Meccanica* **29** (4), 383–391.

Verzicco, R. & Orlandi, P. 1996*a* A finite-difference scheme for three-dimensional incompressible flows in cylindrical coordinates. *J. Comput. Phys.* **123** (2), 402–414.

Verzicco, R. & Orlandi, P. 1996*b* Wall/vortex-ring interactions. *Appl. Mech. Rev.* **49** (10), 447–461.

Walker, J. D. A., Smith, C. R., Cerra, A. W. & Doligaski, T. L. 1987 The impact of a vortex ring on a wall. *J. Fluid Mech.* **181**, 99–140.

Yamada, H., Hochizuki, O., Yamabe, H. & Matsui, T. 1985 Pressure variation on a flat wall induced by an approaching vortex ring. *J. Phys. Soc. Japan* **54** (11), 4151–4160.

Yu, D., Mei, R., Luo, L.-S. & Shyy, W. 2003 Viscous flow computations with the method of lattice Boltzmann equation. *Prog. Aerosp. Sci.* **39** (5), 329–367.

https://doi.org/10.1017/S0022112010002727 Published online by Cambridge University Press